

Bi–Sb Nanocrystals Embedded in Phosphorus as High-Performance Potassium Ion Battery Electrodes

Kuan-Ting Chen and Hsing-Yu Tuan*



Cite This: *ACS Nano* 2020, 14, 11648–11661



Read Online

ACCESS |



Metrics & More



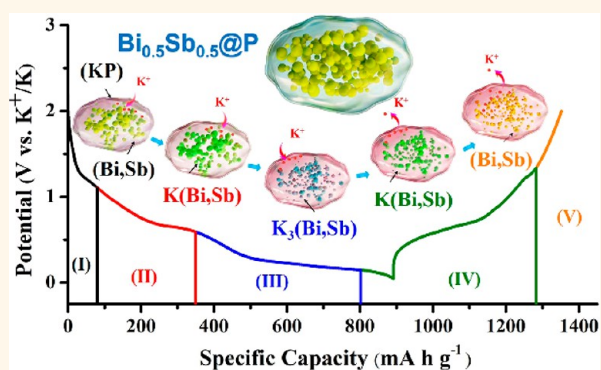
Article Recommendations



Supporting Information

ABSTRACT: The development of high-performance potassium ion battery (KIB) electrodes requires a nanoengineering design aimed at optimizing the construction of active material/buffer material nanocomposites. These nanocomposites will alleviate the stress resulting from large volume changes induced by K^+ ion insertion/extraction and enhance the electrical and ion conductivity. We report the synthesis of phosphorus-embedded ultrasmall bismuth–antimony nanocrystals ($Bi_xSb_{1-x}@P$, ($0 \leq x \leq 1$)) for KIB anodes *via* a facile solution precipitation at room temperature. $Bi_xSb_{1-x}@P$ nanocomposites can enhance potassiation–depotassiation reactions with K^+ ions, owing to several attributes. First, by adjusting the feed ratios of the Bi/Sb reactants, the composition of Bi_xSb_{1-x} nanocrystals can be systematically tuned for the best KIB anode performance. Second, extremely small (diameter ≈ 3 nm) Bi_xSb_{1-x} nanocrystals were obtained after cycling and were fixed firmly inside the P matrix. These nanocrystals were effective in buffering the large volume change and preventing the collapse of the electrode. Third, the P matrix served as a good medium for both electron and K^+ ion transport to enable rapid charge and discharge processes. Fourth, thin and stable solid electrolyte interface (SEI) layers that formed on the surface of the cycled $Bi_xSb_{1-x}@P$ electrodes resulted in low resistance of the overall battery electrode. Lastly, *in situ* X-ray diffraction analysis of K^+ ion insertion/extraction into/from the $Bi_xSb_{1-x}@P$ electrodes revealed that the potassium storage mechanism involves a simple, direct, and reversible reaction pathway: $(Bi, Sb) \leftrightarrow K(Bi, Sb) \leftrightarrow K_3(Bi, Sb)$. Therefore, electrodes with the optimized composition, *i.e.*, $Bi_{0.5}Sb_{0.5}@P$, exhibited excellent electrochemical performance (in terms of specific capacity, rate capacities, and cycling stability) as KIB anodes. $Bi_{0.5}Sb_{0.5}@P$ anodes retained specific capacities of $295.4 \text{ mA h g}^{-1}$ at 500 mA g^{-1} and $339.1 \text{ mA h g}^{-1}$ at 1 A g^{-1} after 800 and 550 cycles, respectively. Furthermore, a capacity of $258.5 \text{ mA h g}^{-1}$ even at 6.5 A g^{-1} revealed the outstanding rate capability of the Sb-based KIB anodes. Proof-of-concept KIBs utilizing $Bi_{0.5}Sb_{0.5}@P$ as an anode and PTCDA (perylene-tetracarboxylic dianhydride) as a cathode were used to demonstrate the applicability of $Bi_{0.5}Sb_{0.5}@P$ electrodes to full cells. This study shows that $Bi_xSb_{1-x}@P$ nanocomposites are promising carbon-free anode materials for KIB anodes and are readily compatible with the commercial slurry-coating process applied in the battery manufacturing industry.

KEYWORDS: potassium, battery, phosphorus, nanotechnology, nanocrystals



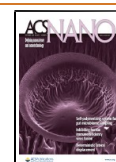
Potassium ion batteries (KIBs) may replace lithium ion batteries (LIBs) as energy storage systems for large-scale stationary energy, owing to several intrinsic advantages. These include high-earth-abundance reserves of K (2.09 wt % in the earth's crust, *i.e.*, 1000 times more abundant than that of Li (0.0017 wt %)), a lower standard reduction potential (-2.93 V) for K^+/K than that for Na^+/Na (-2.71 V) in a nonaqueous electrolyte, and a smaller Stokes radius of K ions (3.6 \AA in polycarbonate) than that of Li ions (4.8 \AA), thereby enabling higher mobility and diffusion kinetics between the electrolyte and electrode.^{1–5} However, it has been challenging to develop electrode materials for high-perform-

ance KIBs, especially for anode materials. K belongs to a family of alkali metals, and the corresponding ion radius (1.38 \AA) is nearly twice as large as that of the Li ion (0.76 \AA).^{5–7} Therefore, K^+ ion insertion/extraction into/from the electrode

Received: May 19, 2020

Accepted: September 4, 2020

Published: September 4, 2020



is more difficult relative to Li^+ and Na^+ ions, leading to slower transport dynamics and a large volume change during potassiation–depotassiation reactions. This resulted in an undesirable cycling performance and a rapid capacity decay. For example, the maximum potassium storage of graphite (KC_8 : 279 mA h g^{-1}), a widely used LIB anode, is too low for KIBs.^{8–11} Unfortunately, only a few materials exhibit the high specific capacities ($>300 \text{ mA h g}^{-1}$) required for KIB anodes.^{12–14}

Antimony (Sb) is considered a promising KIB anode, owing to its extremely high theoretical capacity of 660 mA h g^{-1} while alloying with K to form K_3Sb at room temperatures. However, Sb undergoes a large volume expansion ($\sim 407\%$) when fully alloyed with K, and bulk Sb cannot endure such high stresses with repeated potassiation–depotassiation cycles, resulting in battery failure and electrode material pulverization.^{15–19} The methods developed to address this problem can be grouped into the following three categories. (i) The first category is utilizing carbon materials as a soft and ductile matrix with a minor volume fraction to buffer mechanical stresses/strains and maintain the electrode structure integrity during the alloying and dealloying processes. For example, Sb–C composite materials, such as Sb@G@C ,²⁰ Sb@NPMC ,²¹ Mxene@Sb ,²² Sb@HCT ,²³ and SnSb-G-C ,²⁴ have been reported as Sb–C KIB anodes. (ii) The second category is using Sb–X (X = Sb-based alloy element) compounds as anodes. Sb–X compounds may yield enhanced structural integrity or increased theoretical capacity depending on the intrinsic characteristics of X.^{25–28} Among these alloys, the intermetallic Bi–Sb alloy has received particular attention due to the following advantages. (1) Bi and Sb form a solid solution ($\text{Bi}_x\text{Sb}_{1-x}$) over the entire composition range, and hence, a tunable composition can be adjusted to optimize the electrode performance.^{29–32} (2) The theoretical capacity of Bi is 385 mA h g^{-1} for K^+ ion storage, ensuring high specific capacities of $\text{Bi}_x\text{Sb}_{1-x}$ alloys. (3) The volume expansion of $\text{K}_3(\text{Bi}, \text{Sb})$, 384% ³³ (based on the space group $Fm\bar{3}m$ with a cubic crystal system), is smaller than that of Bi to K_3Bi (406%)³¹ and Sb to K_3Sb (407%).³³ Additionally, recent reports suggested that the introduction of Bi into Sb yields high toughness for antipulverization and long-term durability for Na^+ ion insertion and extraction. This results from the higher B_h/G_h ratios and Poisson ratios of Bi relative to those of Sb metal, which induces considerable lattice softening of Sb, through the so-called lattice softening effect.³⁴ (iii) The third category is that rational designs of nanostructures can enhance structural integrity and electron transport for improved battery performance.³⁵ For example, Wang et al. reported the synthesis of $\text{Bi}_{1.11}\text{Sb}_{0.89}\text{S}_3$ nanotubes as KIB anodes to enable *in situ* alloying of $\text{Bi}_x\text{Sb}_{1-x}$ alloy nanocrystals after efficient insertion and extraction of K^+ ions.³⁶ Xiong et al. reported Bi–Sb@C composite nanosheets synthesized *via* a freeze-drying and pyrolysis method for stable cycling KIB anodes.³³

The selection of buffer materials for the formation of Sb-based composites is necessary for the development of high-performance batteries with stable cycling stability. The reported Sb-based KIB anodes are all in the form of carbon composites used to alleviate stress tension, enhance electrode stability, and increase potassium ion diffusion and electrode conductivity.^{18,37–39} However, the preparation of carbon composites usually requires high temperatures and multiple indirect steps that are mostly associated with complex procedures. Large-scale and reliable synthesis that ensures

stable product quality is also difficult. Furthermore, the large carbon content of the composites suppresses the overall electrode capacity. Furthermore, even in the form of carbon composites, the originally designed nanostructures (e.g., nanopillars or nanotubes) disintegrated or changed shape after repeated insertion/extraction of potassium ions. The active materials after cycling appear as fragments of original materials embedded in the carbon host. This may have resulted from the fact that the reported KIB anode nanostructures have particle sizes or lateral dimensions larger than 100 nm. That is, the sizes are too large to tolerate the stresses associated with these potassiation–depotassiation cycles, and in fact, the reported Sb-based electrodes are unable to sustain good rate performance. Therefore, an alternative nanoengineering design aimed at optimizing the construction of active materials/buffer material nanocomposites for realizing high-performance KIB anodes is necessary.^{40–45}

Herein, we demonstrate a solution-phase precipitation approach to synthesizing phosphorus-embedded $\text{Bi}_x\text{Sb}_{1-x}$ ($0 \leq x \leq 1$) nanocrystals as KIB anodes at room temperature. The reactions occur within several seconds in the presence of BiCl_3 , SbCl_3 , and $\text{P}(\text{SiMe}_3)_3$ *via* reactions involving the elimination of a silyl halide Me_3SiCl . As-synthesized $\text{Bi}_x\text{Sb}_{1-x}$ nanocrystals (average diameter = 6.35 nm) were embedded in the phosphorus matrix, thereby yielding $\text{Bi}_x\text{Sb}_{1-x}@P$ nanocomposites. $\text{Bi}_x\text{Sb}_{1-x}$ nanocrystals with complete stoichiometry tuning can be obtained *via* the developed synthetic route and used for KIB anode examination without forming P–C composites. Therefore, $\text{Bi}_{0.5}\text{Sb}_{0.5}@P$ nanocomposites exhibit very good battery performance with capacities of $295.4 \text{ mA h g}^{-1}$ (cycling rate = 500 mA g^{-1}) and $339.1 \text{ mA h g}^{-1}$ (cycling rate = 1 A g^{-1}) after 800 and 550 cycles, respectively. Furthermore, an excellent rate capability with a capacity of $258.5 \text{ mA h g}^{-1}$ at 6.5 A g^{-1} is obtained, which is the highest among the values reported for Sb-based KIB anodes. TEM images of cycled $\text{Bi}_{0.5}\text{Sb}_{0.5}@P$ electrodes reveal dense ultra-small $\text{Bi}_{0.5}\text{Sb}_{0.5}$ nanocrystals (diameter = 3.39 nm) were formed and were firmly fixed within the P matrix, thus providing reliable structural integrity as well as efficient electron and K^+ ion transport. *In situ* operando XRD of $\text{Bi}_{0.5}\text{Sb}_{0.5}@P$ electrodes indicates that the storage mechanism proceeds through a highly reversible alloying–dealloying reaction: $(\text{Bi}, \text{Sb}) \leftrightarrow \text{K}(\text{Bi}, \text{Sb}) \leftrightarrow \text{K}_3(\text{Bi}, \text{Sb})$. Finally, the performance of the full cell assembled by using $\text{Bi}_{0.5}\text{Sb}_{0.5}@P$ as the anode and PTCDA (perylene-tetracarboxylic dianhydride) as the cathode was evaluated to demonstrate their feasibility for KIBs.

RESULTS AND DISCUSSION

$\text{Bi}_x\text{Sb}_{1-x}@P$ nanocrystals were synthesized *via* a solution precipitation route (see Figure 1). A combination of metal BiCl_3 and SbCl_3 precursors with a desired individual mole ratio is dissolved in toluene. $\text{P}(\text{SiMe}_3)_3$ is used as the P precursor.^{46,47} The reaction is illustrated in Figure 1a. $\text{P}(\text{SiMe}_3)_3$ in hexane is added dropwise from the buret into a stirred solution of BiCl_3 and SbCl_3 in the lower bottle at room temperature. As shown in Figure 1b,c, the reactions occur at 3.2 s when the color of the solution starts to change from yellow to dark black precipitates. $\text{Bi}_x\text{Sb}_{1-x}@P$ alloy particles form *via* the reactions involving the elimination of a silyl halide Me_3SiX (X = Cl, Br, I). $\text{P}(\text{SiMe}_3)_3$ is the key reagent that controls the overall reactions and enables the formation of the P matrix. The synthetic protocol may be

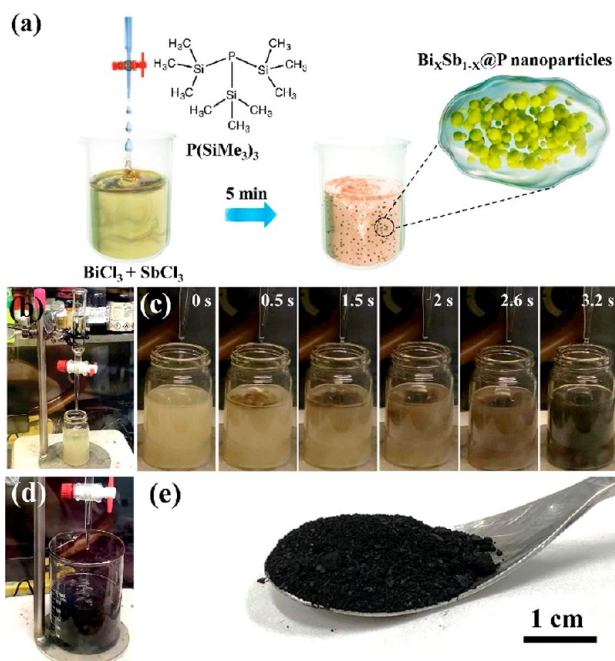


Figure 1. Synthesis of the $\text{Bi}_x\text{Sb}_{1-x}@P$ nanocomposites. (a) Schematic illustration of $\text{Bi}_x\text{Sb}_{1-x}@P$ synthesis, (b) experimental setup, (c) reaction process of $\text{Bi}_x\text{Sb}_{1-x}@P$ nanocomposites via a solution precipitation process lasting for 3.2 s, and (d) large-scale synthesis of $\text{Bi}_x\text{Sb}_{1-x}@P$ nanocomposites. (e) Photograph showing ~ 1 g of $\text{Bi}_{0.5}\text{Sb}_{0.5}@P$ powders obtained from the reaction depicted in (d).

applied to the synthesis of various nanocrystals embedded in the matrix and is quite advantageous for the large-scale production of nanocrystals. Figure 1d shows an experimental setup, where a 300 mL glass beaker is used as a reactor to synthesize ~ 1 g of $\text{Bi}_{0.5}\text{Sb}_{0.5}@P$ nanocrystals in one batch reaction (see Figure 1e).

A representative synthesis result of $\text{Bi}_x\text{Sb}_{1-x}@P$ nanocrystals obtained by reacting 1.72 mmol of individual Bi and Sb reactants for the formation of $\text{Bi}_{0.5}\text{Sb}_{0.5}$ alloy nanocrystals is shown in Figure 2. The XRD pattern of the product and the Rietveld-refined results (shown in Figure 2a) can be due to a rhombohedral phase with the $R\bar{3}m$ (166) space group. The lattice parameters are calculated based on the fitting curve by utilizing the TOPAS V6 software (see Table S1 in the Supporting Information). Furthermore, the diffraction peak positions of the $\text{Bi}_{0.5}\text{Sb}_{0.5}@P$ nanocomposites are slightly lower than the standard peak positions corresponding to Sb powder in the database (PDF# 851324), since larger Bi atoms substitute for the smaller Sb atoms.²⁹ Through the Scherrer equation, $D = K\lambda/(B\cos\theta)$, the crystal domain size is estimated from the XRD pattern.⁴⁸ The peaks occurring at 27.83° , 49.94° , and 57.30° correspond to $D = 8.86$, 7.35 , and 6.76 nm, respectively. No other peaks except the indexed $\text{Bi}_{0.5}\text{Sb}_{0.5}$ pattern peaks are observed, indicating that the P matrix is amorphous. An average crystal size of 7.76 nm is determined from the three peaks considered in the Scherrer equation. An FESEM image of the nanoparticle composite is shown in Figure 2b. The TEM images shown in Figure 2c,d reveal the $\text{Bi}_{0.5}\text{Sb}_{0.5}@P$ nanocrystals with uniformly dispersed $\text{Bi}_{0.5}\text{Sb}_{0.5}$ alloy nanocrystals embedded in the P matrix. A

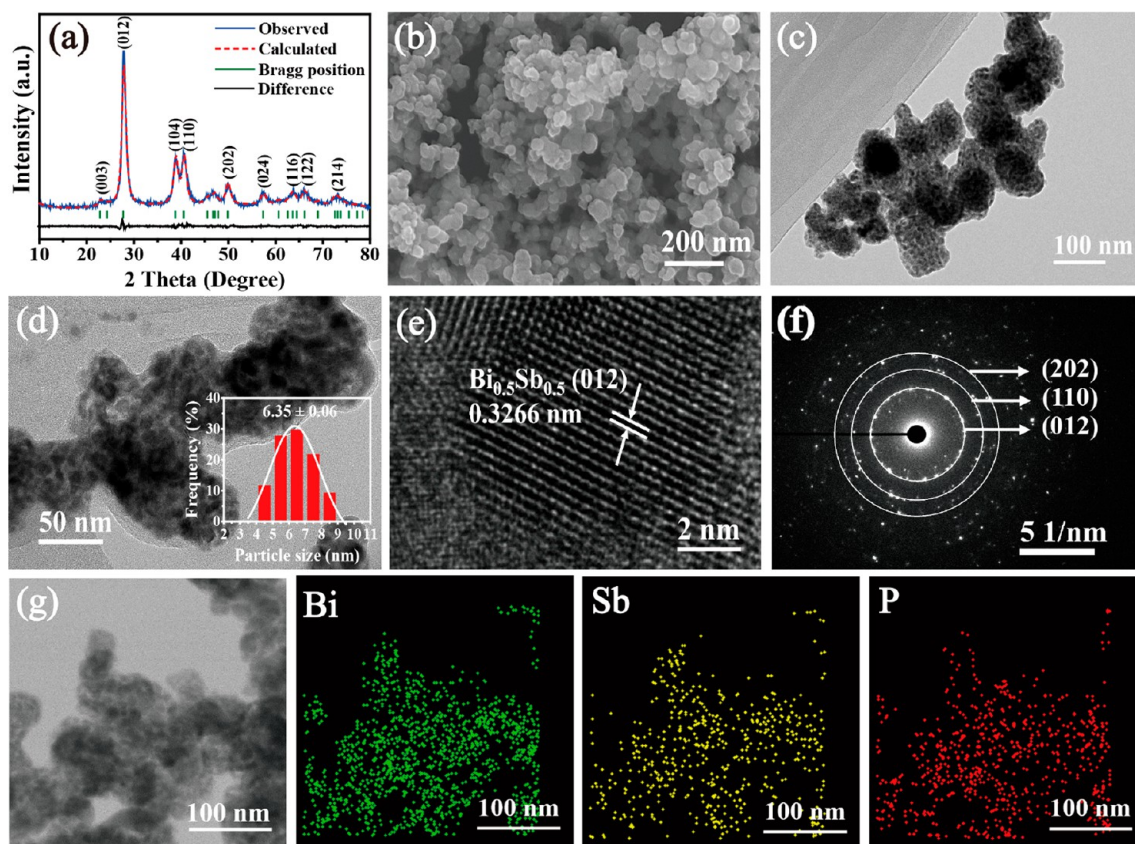


Figure 2. (a) Rietveld refinement of the XRD pattern. (b) SEM, (c,d) TEM, and (e) HRTEM images of the $\text{Bi}_{0.5}\text{Sb}_{0.5}@P$ nanocomposites. (f–g) SAED pattern and EDS mapping obtained for a field of particles.

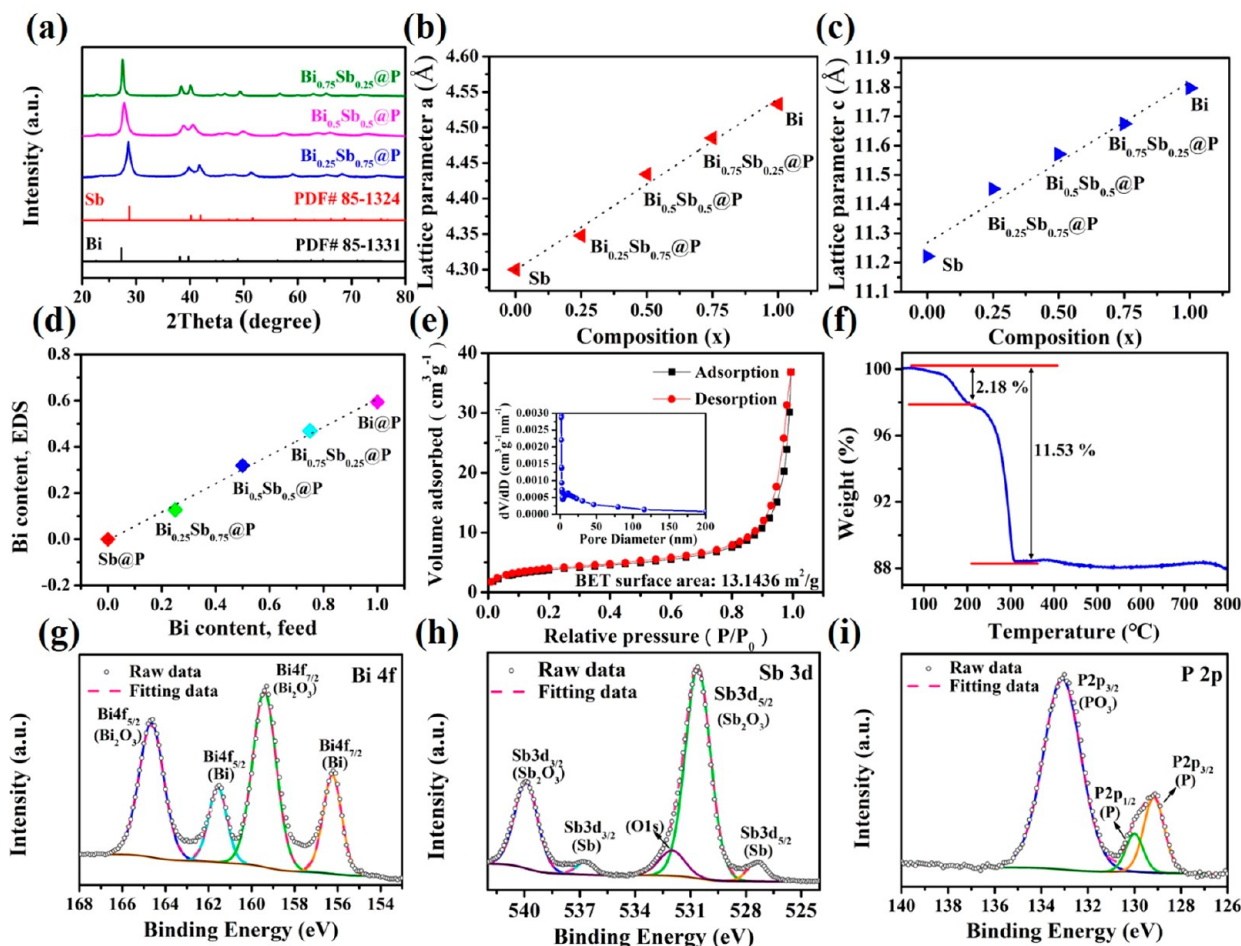


Figure 3. (a) XRD patterns of $\text{Bi}_x\text{Sb}_{1-x}@P$ nanocomposites. Dependence of the lattice parameters (b) a and (c) c on x of the $\text{Bi}_x\text{Sb}_{1-x}@P$ nanocomposites. (d) Relationship between the Bi molar contents and the feed versus those in the product determined from the signals of TEM–EDS spectra. (e) N_2 adsorption–desorption isotherm and corresponding pore size distribution (insets) of the $\text{Bi}_{0.5}\text{Sb}_{0.5}@P$ nanocomposites. (f) TGA measurement of the $\text{Bi}_{0.5}\text{Sb}_{0.5}@P$ nanocomposites. High-resolution XPS spectra of (g) Bi 4f, (h) Sb 3d, and (i) P 2p for $\text{Bi}_{0.5}\text{Sb}_{0.5}@P$.

polydispersity of the nanocrystals (average diameter = 6.35 nm) is observed. Figure 2e shows a high-resolution TEM image of a nanocrystal with a single-crystal structure and interplanar d -spacings of 3.26 Å corresponding to the (012) plane of $\text{Bi}_{0.5}\text{Sb}_{0.5}$. The selected-area electron diffraction pattern obtained for a field of the nanocrystals consists of three diffraction rings corresponding to the (202), (110), and (012) planes of $\text{Bi}_{0.5}\text{Sb}_{0.5}$. Furthermore, EDS of these nanocrystals (see Figure S2g,h in the Supporting Information) reveals an average Bi/Sb composition that corresponds closely to the target atomic ratio of 1:1. The P content of $\text{Bi}_{0.5}\text{Sb}_{0.5}@P$ is ~9.59 wt %. The elemental mapping spectra further confirm the homogeneous distribution of Sb and Bi in the alloy particles (Figure 2g), consistent with a material of composition close to $\text{Bi}_{0.5}\text{Sb}_{0.5}$.

The developed synthetic route can lead to obtaining $\text{Bi}_x\text{Sb}_{1-x}@P$ nanocrystals with a stoichiometry-adjusted composition tuning from $x = 0$ to 1 by varying the molar ratios of the Bi/Sb feed reactants. Sb and Bi belong to the same space group ($R\bar{3}m$) and form a completely mixed solid solution (since they are isostructural), as revealed by the phase diagram. The synthesis produces no other measurable phases. Figure 3a shows the XRD patterns of $\text{Bi}_x\text{Sb}_{1-x}@P$ nanocrystals synthesized from separate Bi/Sb molar ratios of 3:1, 1:1, and

1:3. At $x = 0$, the spectrum corresponds to that of Sb (PDF# 851324). As the Bi content increases, the diffraction peaks gradually shift toward a lower 2θ angle due to the substitution of Bi atoms (radius = 2.3 Å), which are smaller than the Sb atoms (radius = 2.06 Å). The lattice parameters (a and c) calculated from XRD patterns are listed in Table S2 in the Supporting Information. The lattice parameters as a function of x in $\text{Bi}_x\text{Sb}_{1-x}@P$ are plotted in Figure 3b,c. The lattice spacing increases along the a -axis (from 4.3 Å (Sb) to 4.53 Å (Bi)) and c -axis (from 11.22 Å (Sb) to 11.79 Å (Bi)) with decreasing Sb content of the nanocrystals. At $x = 1$, the XRD data can be indexed to Bi (PDF# 851331). The lattice parameters are linearly related to the Sb content, which is consistent with Vegard's law,⁴⁹ *i.e.*, Bi–Sb is homogeneously distributed in the alloyed nanocrystals. Furthermore, EDS conducted for a field of $\text{Bi}_x\text{Sb}_{1-x}@P$ nanocomposites (Figure 3d) with varying compositions reveals a linear trend similar to that observed from the XRD pattern. The obtained elemental Sb ratio of the $\text{Bi}_x\text{Sb}_{1-x}@P$ nanocrystals is very close to that of the initial Bi/Sb molar ratio of the feed reactants. Figure 3e shows the Brunauer–Emmett–Teller measurements of the $\text{Bi}_{0.5}\text{Sb}_{0.5}@P$ nanocrystals. The specific surface area ($13.14 \text{ m}^2 \text{ g}^{-1}$) is determined from the Kelvin equation associated with the Barrett–Joyner–Halenda method based on the adsorption

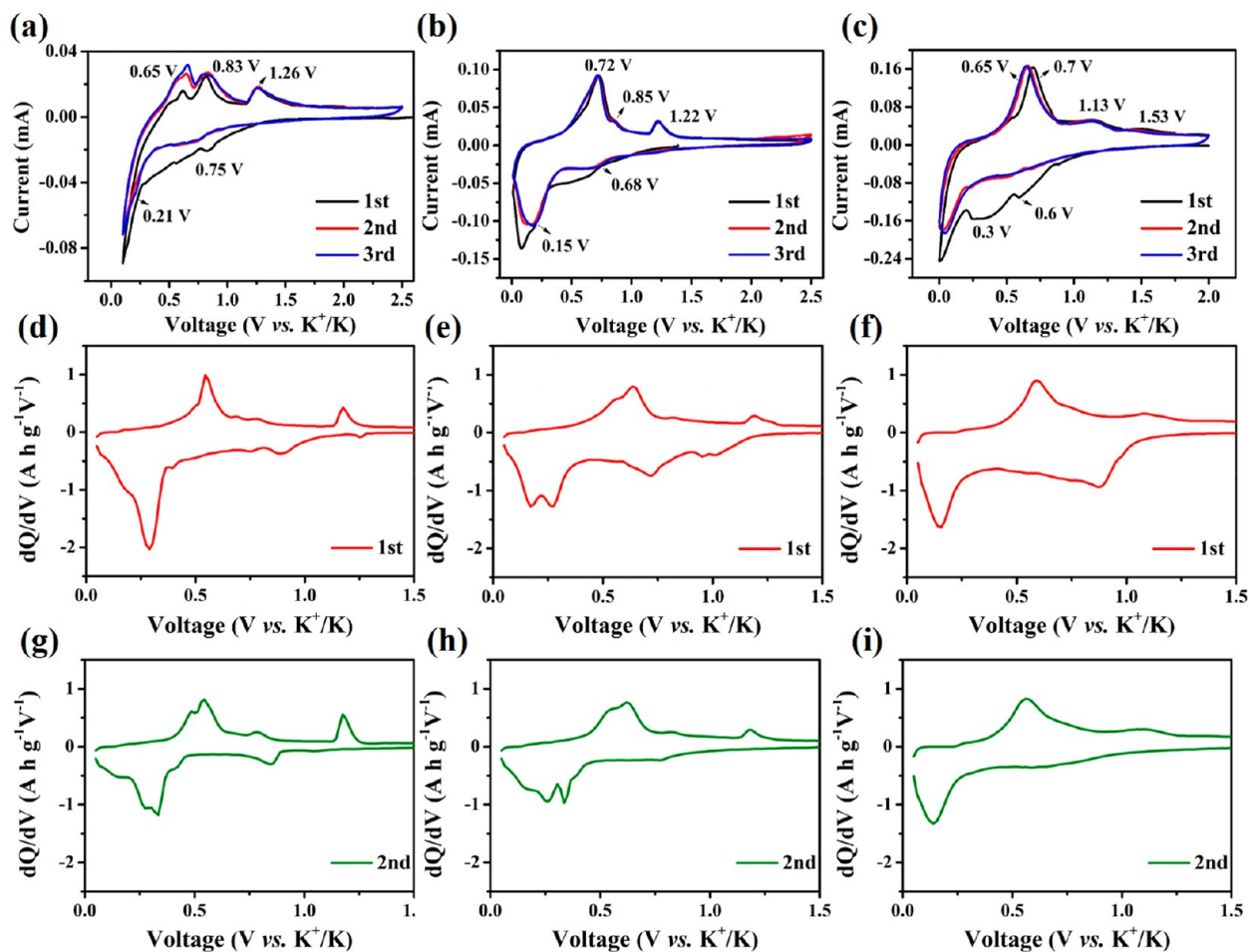


Figure 4. (a–c) Initial three-cycle cyclic voltammetry curves obtained at a scan rate of 0.1 mV s^{-1} . Differential capacity plots obtained for the (d–f) first and (g–i) second cycles of $\text{Bi}_{0.5}\text{Sb}_{0.5}@P$ nanocomposites.

branches of the isotherms, and characteristics of a typical nanocrystal surface area are observed. The TGA (Figure 3f) result reveals a first sharp weight loss (2.18 wt %) at 150 to 200 °C, corresponding to residue Me_3SiX in the product. A second sharp weight loss (9.35 wt %) at 300 °C corresponding to the weight loss of P in the nanocrystals is also observed. The P weight loss is very close to the P content of $\text{Bi}_{0.5}\text{Sb}_{0.5}@P$ (~9.59 wt %) detected from the EDS spectrum (Figure S2). The chemical electronic state of the $\text{Bi}_{0.5}\text{Sb}_{0.5}@P$ nanocrystals is investigated using X-ray photoelectron spectroscopy (XPS). All binding energies have been corrected by referencing the C 1s (284.6 eV). Figure 3 shows the XPS spectra of the $\text{Bi}_{0.5}\text{Sb}_{0.5}@P$ powder. Figure 3g shows the Bi $4f_{5/2}$ and Bi $4f_{7/2}$; $4f$ core splitting into Bi $4f_{5/2}$ (161.6 eV) and Bi $4f_{7/2}$ (156.3 eV) peaks with a peak separation of 5.3 eV is also observed.⁵⁰ Furthermore, Bi_2O_3 $4f_{7/2}$ (159.4 eV) and Bi_2O_3 $4f_{5/2}$ (164.7 eV) are generated by the formation of oxides.⁵¹ The peaks located at 536.8 and 527.3 eV with a peak separation of 6.2 eV (Figure 3h) are due to Sb $3d_{3/2}$ and Sb $3d_{5/2}$, respectively.⁵² The binding energies of Sb $3d_{3/2}$ and Sb $3d_{5/2}$ are lower than the standard Sb_2O_3 $3d_{3/2}$ (539.9 eV) and Sb_2O_3 $3d_{5/2}$ (530.6 eV) values. This reconfirms the formation of oxides (Bi_xO_y and Sb_xO_y) on the surface of the $\text{Bi}_{0.5}\text{Sb}_{0.5}@P$ composites.^{16,33} However, no oxides are detected *via* the XRD measurement, indicating that only a few amorphous surface oxides are formed. The P 2p (Figure 3i) spectrum consists of peaks

corresponding to P $2p_{3/2}$ (133.1 eV) for PO_3 , P $2p_{1/2}$ (130 eV) for P, and P $2p_{3/2}$ (129.16 eV)^{53,54} for P.

The results in Figure 4a–c show the cyclic voltammetry (CV) plots of $\text{Bi}@P$, $\text{Bi}_{0.5}\text{Sb}_{0.5}@P$, and $\text{Sb}@P$ nanocomposites, respectively, for the initial three cycles at a scan rate of 0.1 mV s^{-1} between 0.01 and 2.5 V (*vs* K^+/K). In the first cathodic scan, the initial cathodic process is characterized by a peak at ~0.7 V and a broad curve from 0.30 to 0.08 V, which is weakened during the subsequent cycles. The peaks can be attributed to the potassiation of Bi and the formation of a solid electrolyte interface (SEI) layer on the electrode surface *via* electrolyte decomposition. The irreversible cathodic peak near 0.1 V can be attributed to the irreversible reaction of the oxides (Bi_xO_y and Sb_xO_y) on the surface of the $\text{Bi}_{0.5}\text{Sb}_{0.5}$ alloy nanocrystals.³³ In the second and third scans, two cathodic peaks occur at 0.68 and 0.15 V, indicating the formation of $\text{K}(\text{Bi}, \text{Sb})$ and $\text{K}_3(\text{Bi}, \text{Sb})$ phases, respectively, which are due to $\text{K}(\text{Bi}, \text{Sb})$ alloy reactions. In the anodic scans, three peaks at 0.72, 0.85, and 1.22 V correspond to the depotassiation reactions of $\text{K}_3(\text{Bi}, \text{Sb}) \rightarrow \text{K}(\text{Bi}, \text{Sb}) \rightarrow (\text{Bi}, \text{Sb})$. The CV curves obtained for the second and third scans overlap strongly, indicating the high reversibility and stability of the $\text{Bi}_{0.5}\text{Sb}_{0.5}@P$ composite anode.^{33,36} Furthermore, the two clear peaks at 0.17 and 0.27 V in the homologous differential capacity (dQ/dV) diagram of the $\text{Bi}_{0.5}\text{Sb}_{0.5}@P$ nanocrystals during the first discharge suggests a two-step reduction process (Figure 4e). The peak voltage at 0.17 V is slightly right shifted

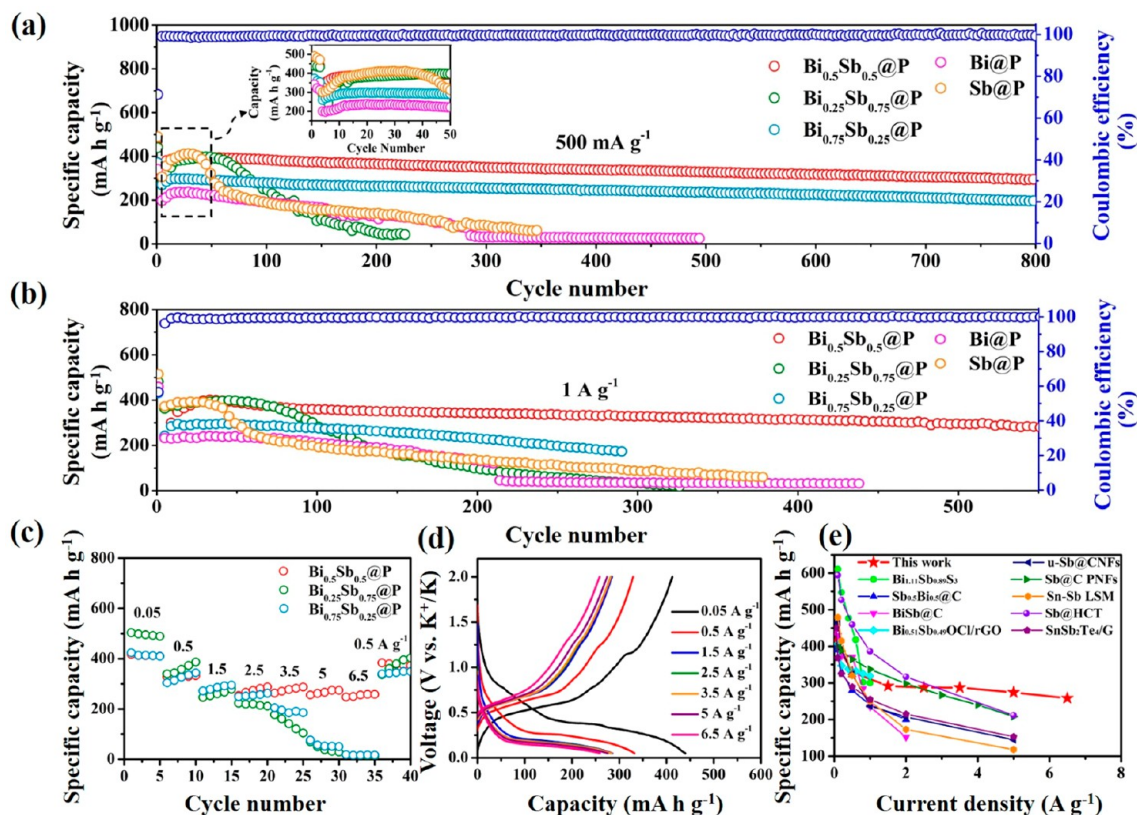


Figure 5. Electrochemical performance of $\text{Bi}_x\text{Sb}_{1-x}@P$ nanocomposites. Cycling performance of $\text{Bi}_x\text{Sb}_{1-x}@P$ electrodes at rates of (a) 500 mA g^{-1} and (b) 1 A g^{-1} . (c,d) Rate performance and corresponding voltage profiles of $\text{Bi}_x\text{Sb}_{1-x}@P$ electrode at rates increased from 0.05 to 6.5 A and then reduced to 0.5 A . (e) Rate capabilities of $\text{Bi}_x\text{Sb}_{1-x}@P$ compared with those of Sb-based KIB anode materials reported in the literature.^{17,18,23,26,31–33,36,55}

to the voltage of $\text{Sb}@C$ (Figure 4f) at 0.15 V , whereas the other voltage at 0.27 V is slightly left shifted to the peak voltage of $\text{Bi}@C$ at 0.29 V (Figure 4d). This indicates a two-step potassiation reaction of Bi and Sb: $(\text{Bi}, \text{Sb}) \rightarrow \text{K}(\text{Bi}, \text{Sb}) \rightarrow \text{K}_3(\text{Bi}, \text{Sb})$. In the second cycle (Figure 4g–i), a similar two-step potassiation reaction is observed. The two oxidation peaks at 0.62 and 1.18 V in the first two cycles correspond to a two-step depotassiation reaction: $\text{K}_3(\text{Bi}, \text{Sb}) \rightarrow \text{K}(\text{Bi}, \text{Sb}) \rightarrow (\text{Bi}, \text{Sb})$.^{32,33}

In the half cell test, metal potassium and 4 M bis-(fluorosulfonyl)imide (KFSI) potassium are used as the counter electrode and the electrolyte in dimethyl ether (DME), respectively. A high concentration of electrolytes (e.g., 5 M KFSI in DME) can form a more stable SEI membrane (than that formed by a low concentration),³⁶ allowing K^+ ion electrodes to maintain long-term stability. Recent reports have shown that the synergistic interaction between Bi atoms and Sb atoms can produce a buffering effect that mitigates structural changes induced by volume changes during the potassiation–depotassiation process and improve cycle stability.³¹ Through the developed synthetic approach that allows stoichiometric control of nanocrystals, the optimally tuned Bi–Sb composition can maximize the synergistic effect of Bi–Sb.^{29,36} The initial discharge/charge curves of the $\text{Bi}@P$, $\text{Bi}_{0.25}\text{Sb}_{0.75}@P$, $\text{Bi}_{0.5}\text{Sb}_{0.5}@P$, $\text{Bi}_{0.75}\text{Sb}_{0.25}@P$, and $\text{Sb}@P$ electrodes at 50 mA g^{-1} (first discharge capacities: 341.4 , 439.9 , 444.7 , 371.4 , and $490.1 \text{ mA h g}^{-1}$, respectively) are shown in Figure 5a. The irreversible capacities of the first cycle result from the formation of an SEI film on the electrode surface. After three cycles at 50 mA g^{-1} , the current

rate is changed to 500 mA g^{-1} to examine the cycling stability of the five electrodes. After the 50 cycles, all five electrodes exhibit fairly stable capacity performance (Figure 5a, inset). The capacities of $\text{Bi}_{0.5}\text{Sb}_{0.5}@P$ and $\text{Bi}_{0.25}\text{Sb}_{0.75}@P$ (393.6 and $397.6 \text{ mA h g}^{-1}$, respectively) are higher than those of $\text{Bi}_{0.75}\text{Sb}_{0.25}@P$ ($291.1 \text{ mA h g}^{-1}$), $\text{Bi}@P$ ($221.6 \text{ mA h g}^{-1}$), and $\text{Sb}@P$ ($312.4 \text{ mA h g}^{-1}$). If 800 cycles are considered, quite different cycling stability is observed. That is, $\text{Bi}_{0.5}\text{Sb}_{0.5}@P$ and $\text{Bi}_{0.75}\text{Sb}_{0.25}@P$ exhibit a very stable 800th-cycle cycling performance with respective capacities of 295.4 and $195.5 \text{ mA h g}^{-1}$, corresponding to capacity decays of only 0.12 and 0.13 per cycle. This behavior differs remarkably from that of the other three electrodes where a significant decline occurs after around the 100th cycle. In fact, another $\text{Bi}_{0.5}\text{Sb}_{0.5}@P$ electrode retains cycling stability up to 1000 cycles but delivers a slightly decreased capacity of 192 mA h g^{-1} (see Figure S8 in the Supporting Information). The 1000th-cycle stability is comparable with those recently reported for K^+ ion electrodes using $\text{Bi}_{1.11}\text{Sb}_{0.89}\text{S}_3$ nanotube and $\text{Bi}_{0.51}\text{Sb}_{0.49}\text{OCl/rGO}$ composites^{32,36} (see Figure S5d in the Supporting Information for the corresponding discharge/charge curve of $\text{Bi}_{0.5}\text{Sb}_{0.5}@P$). Similar polarization curves are obtained for the charge and discharge curves after 50 cycles. We also examine the electrochemical performance of all five electrodes at 1 A g^{-1} . $\text{Bi}_{0.5}\text{Sb}_{0.5}@P$ is the only electrode that can maintain a lifetime of 550 cycles (Figure 5b), i.e., the other four electrodes exhibit a significant decline after 100 cycles. Furthermore, we also evaluate the performance of $\text{Bi}_{0.5}\text{Sb}_{0.5}@P$, $\text{Bi}_{0.25}\text{Sb}_{0.75}@P$, and $\text{Bi}_{0.75}\text{Sb}_{0.25}@P$ electrodes at various current densities ranging from 0.05 to 6.5 A g^{-1} (Figure 5c). The results reveal that $\text{Bi}_{0.5}\text{Sb}_{0.5}@P$ can

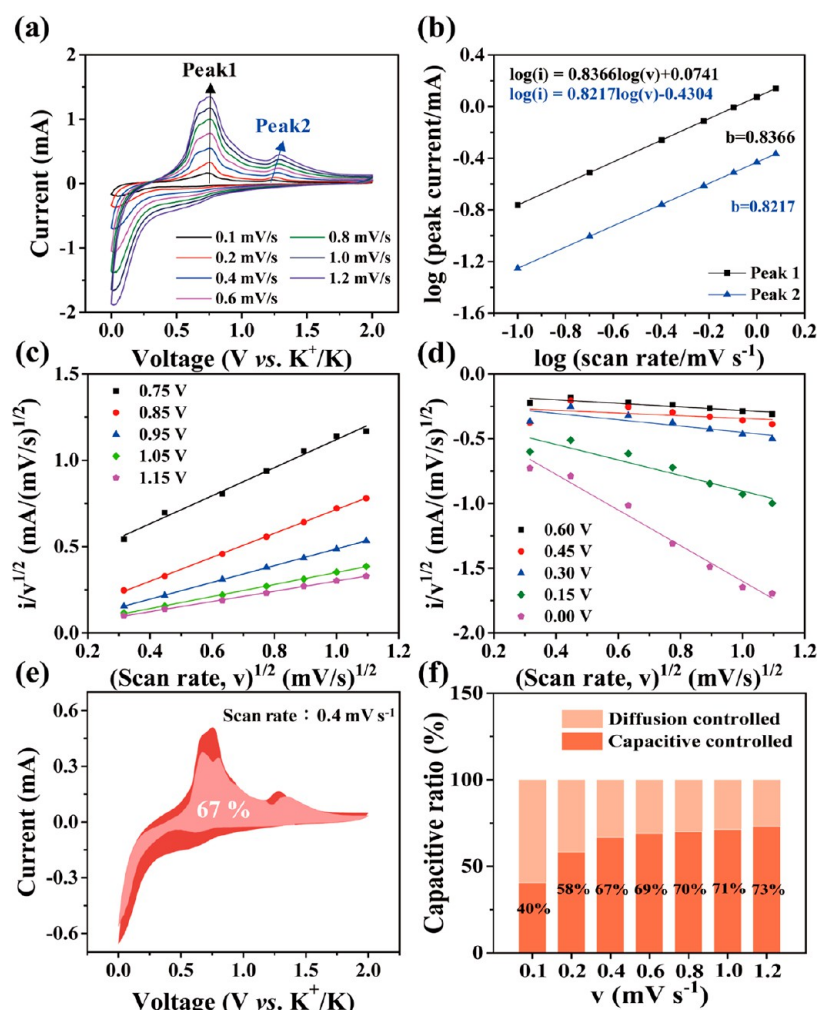


Figure 6. Kinetic analysis of the $\text{Bi}_{0.5}\text{Sb}_{0.5}\text{@P}$ electrode. (a) CV curves at different scan rates. (b) Log (peak current) versus log (scan rate) plot of cathodic/anodic peaks from CV scans and b -value determination lines. (c–d) Plots of $i/v^{1/2}$ versus $v^{1/2}$ used for calculating constants k_1 and k_2 at different potentials. Pseudocapacitive charge storage contributions at a scan rate of (e) 0.4 mV s^{-1} and (f) different scan rates.

maintain a capacity of $\sim 258.5 \text{ mA h g}^{-1}$ even at a current density of 6.5 A g^{-1} . However, $\text{Bi}_{0.25}\text{Sb}_{0.75}\text{@P}$ and $\text{Bi}_{0.75}\text{Sb}_{0.25}\text{@P}$ can only deliver capacities at current rates of up to 3.5 A g^{-1} . When the current density is returned to 0.5 A g^{-1} , all three electrodes return to their original capacity ($\sim 375 \text{ mA h g}^{-1}$) and maintain a stable performance for the subsequent cycles. Figures S5d and S7 show the corresponding discharge/charge curves of the $\text{Bi}_{0.5}\text{Sb}_{0.5}\text{@P}$ electrode at various current densities. At higher currents, voltage polarization will be more pronounced (than at lower currents) because of rapid K^+ ion transport into the electrode. The specific capacities at various current densities of the $\text{Bi}_{0.5}\text{Sb}_{0.5}\text{@P}$ and other Sb-based anodes evaluated in a nonaqueous potassium ion system are compared in Figure S5e. As shown in the figure, the rate capacity of $\text{Bi}_{0.5}\text{Sb}_{0.5}\text{@P}$ surpasses all the capacities reported in the literature (see Table S3 for further details).^{17,18,23,26,31–33,36,55} The above electrochemical testing results indicate that the $\text{Bi}_{0.5}\text{Sb}_{0.5}$ is the optimal chemical component for obtaining the best electrochemical performance of our system.

The high rate capability of the $\text{Bi}_{0.5}\text{Sb}_{0.5}\text{@P}$ electrode was investigated *via* electrochemical kinetic analysis. The CV electrode of $\text{Bi}_{0.5}\text{Sb}_{0.5}\text{@P}$ operated from 0.1 to 1.2 mV s^{-1} is

shown in Figure 6a. The CV curve remains unchanged with changes in the scan rate. The capacitance effect can be determined from the curve, based on the relationship between the measured peak current (i) and the scan rate, (v), *i.e.*, $i = av^b$, where a and b are adjustable constants. Furthermore, the value of b approaches 0.5 or 1.0 , depending on the slope of the logarithmic i versus logarithmic v curve (Figure 6b). For b , values close to 0.5 and 1.0 are obtained for a diffusion-controlled capacitive process and a surface-capacitance-based capacitive process, respectively.^{56,57} The b values obtained for the $\text{Bi}_{0.5}\text{Sb}_{0.5}\text{@P}$ electrode (0.82 and 0.83) indicate that the capacitance dynamics of the electrode is dominated by the surface capacitance. Analyzed using the equation derived by Dunn et al.,⁵⁸ the scan-rate-dependent CV curve was used to quantify the contribution of capacitive effects (surface pseudocapacitance and double-layer capacitance) and diffusion-controlled K^+ ion insertion. The current equation is given as follows

$$i(V) = k_1v + k_2v^{1/2}$$

This equation can be rewritten as

$$i(V)/v^{1/2} = kv^{1/2} + k_2$$

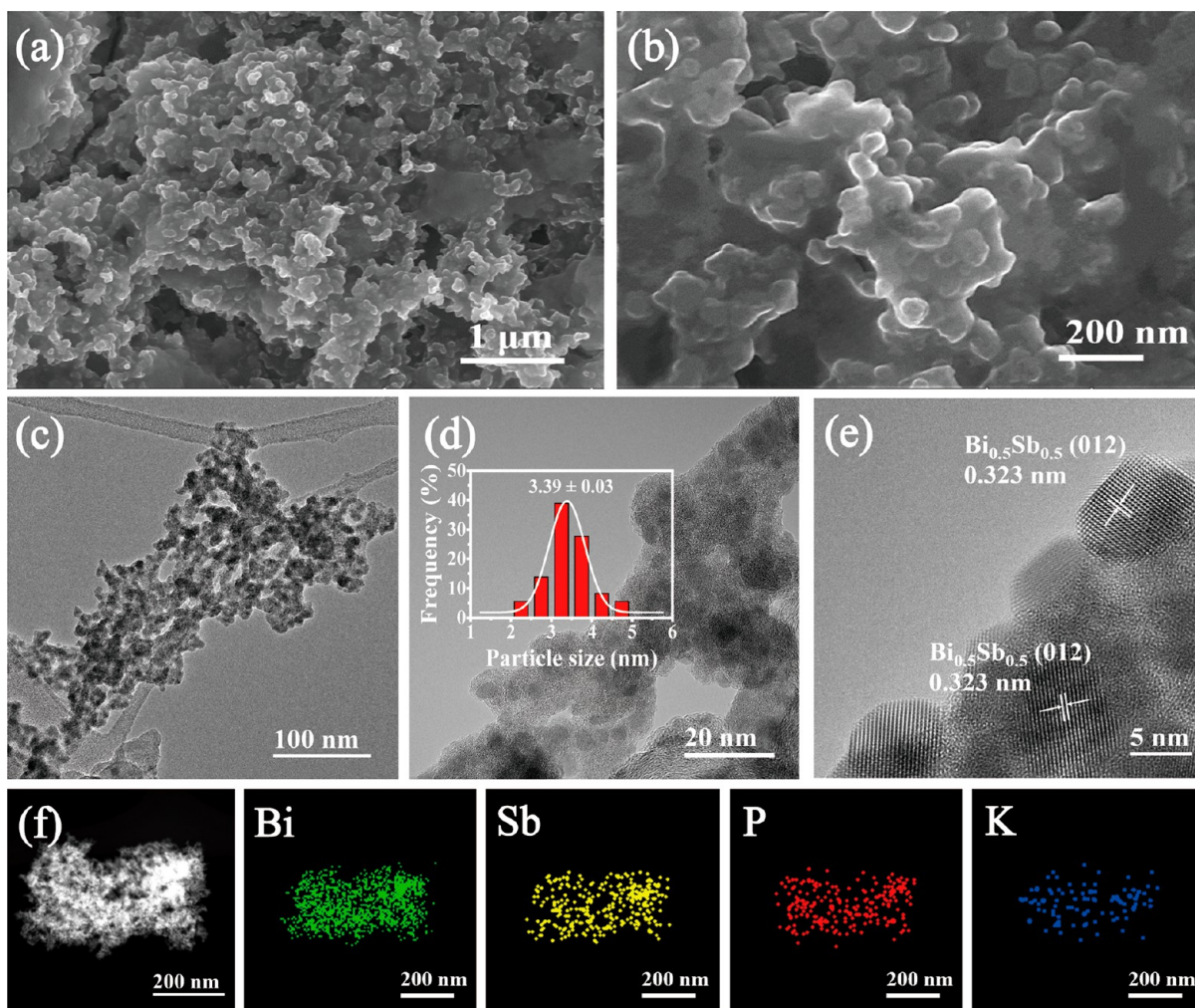


Figure 7. (a,b) SEM, (c,e) HRTEM, and (f) elemental mapping images of Bi, Sb, P, and K of the $\text{Bi}_{0.5}\text{Sb}_{0.5}\text{@P}$ nanocomposites after 550 cycles. Inset: Size distribution histogram corresponding to (d).

where $i(V)$, $k_1\nu$, and $k_2\nu^{1/2}$ represent the capacitive reaction (current–capacitance effect due to the surface) and diffusion-controlled reaction (the current insertion process due to diffusion-controlled K^+) at a given potential V . By plotting $i(V)/\nu^{1/2}$ and $\nu^{1/2}$ at different potentials, a straight line for the values of k_1 (slope) and k_2 (intercept) can be obtained from the above formula. This allows quantification of the insertion current for capacitive effects and diffusion control at a given potential (Figure 6c,d). After the closed CV region is integrated, the number of stored charges in different energy storage modes can be distinguished. A CV curve of 0.4 mV s^{-1} is used for comparison. In Figure 6e, the potential curve (pink area) of the capacitance effect current response is compared with the total measured current area. The $\text{Bi}_{0.5}\text{Sb}_{0.5}\text{@P}$ nanocomposite electrodes are characterized by a large amount of pseudocapacitive charge. The percentage of capacitance contribution relative to the total area is 67% at 0.4 mV s^{-1} , and the total capacitance is mainly a capacitive contribution. Furthermore, capacitive percentages of 40, 58, 67, 69, 70, 71, and 73% are obtained for scan rates of 0.1, 0.2, 0.4, 0.6, 0.8, 1.0, and 1.2 mV s^{-1} , respectively (Figure 6f). This result shows that the major portion of the capacitance from the $\text{Bi}_{0.5}\text{Sb}_{0.5}\text{@P}$ composite electrode is induced by the surface-capacitance effect, which may be due to the P matrix. That is, the matrix yields significant improvement in the capacitance effect of the

entire electrode surface, thereby improving the reactivity of $\text{Bi}_{0.5}\text{Sb}_{0.5}\text{@P}$ with K^+ ions and the charge collection efficiency. Electrochemical impedance spectroscopy was conducted during cycling to understand the inherent properties of the $\text{Bi}_{0.5}\text{Sb}_{0.5}\text{@P}$ composites. The Nyquist plots of $\text{Bi}_{0.5}\text{Sb}_{0.5}\text{@P}$ at different cycles are shown in Figure S9 in the Supporting Information. The resistance of $\text{Bi}_{0.5}\text{Sb}_{0.5}\text{@P}$ decreases gradually with a gradually decreasing size of the $\text{Bi}_{0.5}\text{Sb}_{0.5}$ nanoparticles after 10, 50, and 100 cycles. The decreased resistance can enhance the ionic conductivity of the composite, which is beneficial for the insertion/extraction of K^+ ions into/from the anodes.⁵⁹

Additionally, we also investigate the morphology and crystal structure of the $\text{Bi}_{0.5}\text{Sb}_{0.5}\text{@P}$ electrode after 550 cycles. Figure 7a,b shows SEM images of the electrode after the cycles. These images reveal that the structures are still very compact and are almost identical to those of the electrode before the cycle (Figure S10 in the Supporting Information). In Figure 7b, the electrode surface is uniformly covered by a very thin SEI layer even after hundreds of cycles, indicating considerable SEI stability at the interface between the $\text{Bi}_{0.5}\text{Sb}_{0.5}\text{@P}$ and the liquid electrolyte. The SEI layer is not only an electronic insulator but also a conductor for K^+ ion transport, and hence, a stable SEI layer is critical for achieving a long cycle life. A thick SEI generally results in the consumption of the

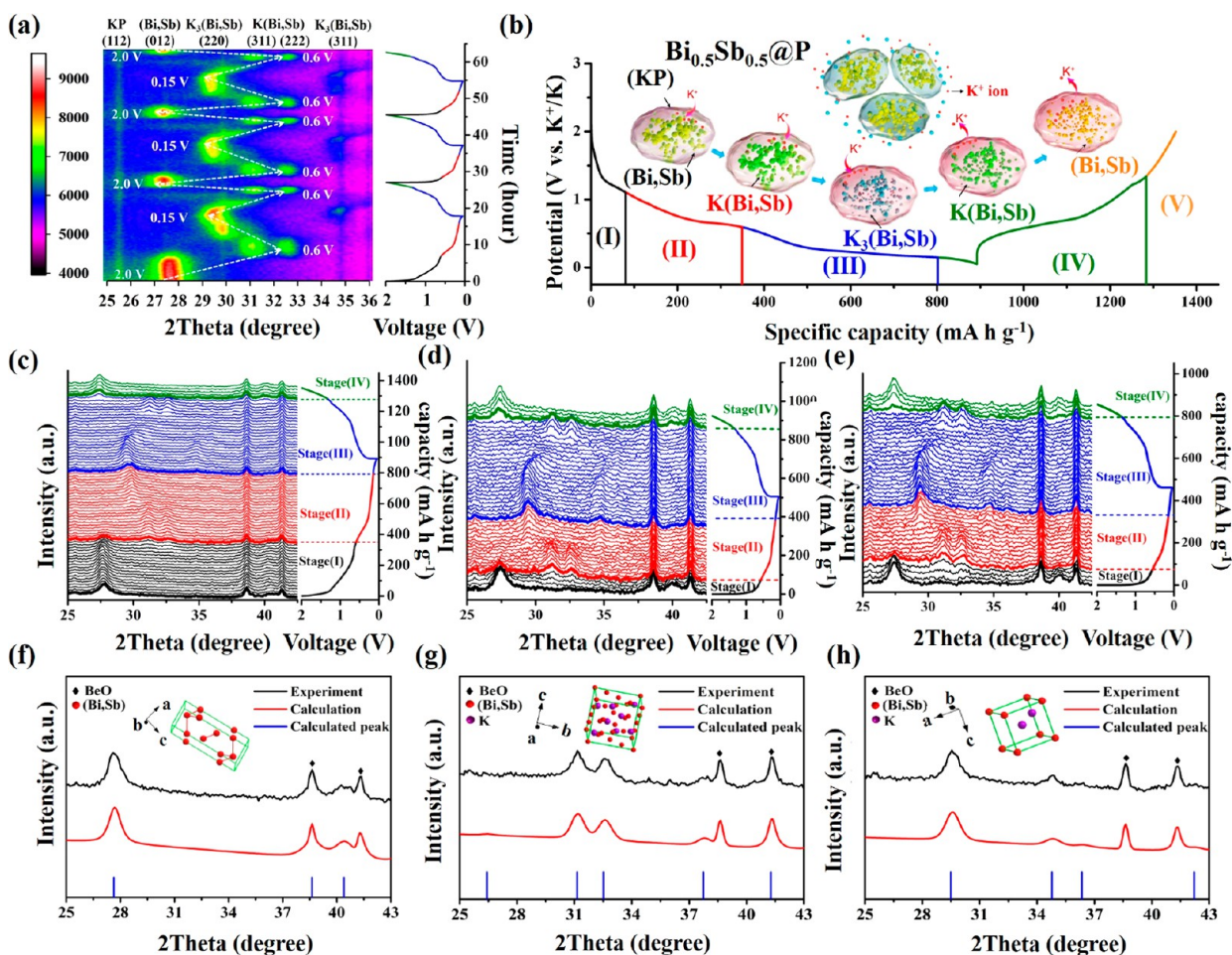


Figure 8. (a) *In situ* contour plot of the operando XRD results obtained for the initial three-cycle potassiation–depotassiation processes of the $\text{Bi}_{0.5}\text{Sb}_{0.5}@P$ electrode. (b) Schematic showing the proposed reaction mechanism during the charge/discharge process (c–e) line plots of the *in situ* XRD results. (f–h) Experimental and calculation results of XRD patterns and corresponding atomic structures (f) (Bi, Sb), (g) K(Bi, Sb), and (h) $\text{K}_3(\text{Bi, Sb})$.

electrolyte and K^+ ions, a large electrical contact resistance between the current collector and anode materials, and a long K^+ ion diffusion distance. This leads to electrode material degradation due to a large mechanical stress. Furthermore, TEM images (Figure 7c,d) show that the $\text{Bi}_{0.5}\text{Sb}_{0.5}$ alloy nanocrystals (average size is only 3.39 nm smaller than that of the original nanocrystals (6.35 nm)) are still densely distributed in the P matrix. The size variation of the nanocrystals is also narrower than that of the noncycled electrode (Figure S11). This result shows that, when K^+ ions react with nanocrystals, the stress resulting from the volume change leads to no cracking of the $\text{Bi}_{0.5}\text{Sb}_{0.5}$ particles, thereby yielding well-distributed nanocrystals embedded in the P matrix. The derived structure is very stable for hundreds of cycles during the alloying–dealloying process. Additionally, the nanocrystals after cycling are single crystalline. The HRTEM image clearly shows that the lattice fringes with a pitch of 0.323 nm correspond to the (012) surface facet of the $\text{Bi}_{0.5}\text{Sb}_{0.5}$ phase (Figure 7e). Furthermore, EDS mapping of the cycled $\text{Bi}_{0.5}\text{Sb}_{0.5}@P$ nanostructures (see Figure 7f) reveals an even distribution of Bi, Sb, P, and K elements in this electrode. This distribution is very similar to that of the original $\text{Bi}_{0.5}\text{Sb}_{0.5}@P$ composite materials.

Therefore, the P matrix plays an important role in the excellent electrochemical performance of the $\text{Bi}_{0.5}\text{Sb}_{0.5}@P$

nanocomposites. The matrix controls and limits the growth of $\text{Bi}_{0.5}\text{Sb}_{0.5}$ nanocrystals to sizes of <10 nm. Despite the large volume change occurring during potassium and depotassium processes, these nanocrystals are firmly immobilized inside the matrix, and the derived $\text{Bi}_{0.5}\text{Sb}_{0.5}@P$ nanocomposites, *i.e.*, P-embedded ultrasmall $\text{Bi}_{0.5}\text{Sb}_{0.5}$ nanoparticles, provide excellent structural advantages for achieving electrochemical stability. Such small nanocrystals (diameters = 3–4 nm) play a critical role in buffering the volume changes, thereby increasing the electrode cycle life and allowing rapid reaction of K^+ ions with $\text{Bi}_{0.5}\text{Sb}_{0.5}$. Furthermore, the P matrix is an efficient medium for both electron and K^+ ion transport and hence enables good rate capability. Additionally, the controlled growth of a thin and stable SEI layer grown on the surface of the matrix also reduces the overall electrode resistance.

The structural advantages of $\text{Bi}_x\text{Sb}_{1-x}@P$ as KIB electrodes compared with other $\text{Bi}_{0.5}\text{Sb}_{0.5}$ materials are investigated. We prepared $\text{Bi}_{0.5}\text{Sb}_{0.5}$ powders using a ball milling method (SEM image and XRD pattern are shown in Figures S12 and S13 in the Supporting Information) and conducted electrochemical characterization, including CV and half cell tests. From the CV diagram (see Figure S14), the shoulders at peak 1 (~0.75 V) and peak 2 (~1.25 V) are relatively wide. Additionally, many unrecognizable peaks appear in the first-cycle dQ/dV diagram of the ball-milled $\text{Bi}_{0.5}\text{Sb}_{0.5}$. The electrochemical reaction of

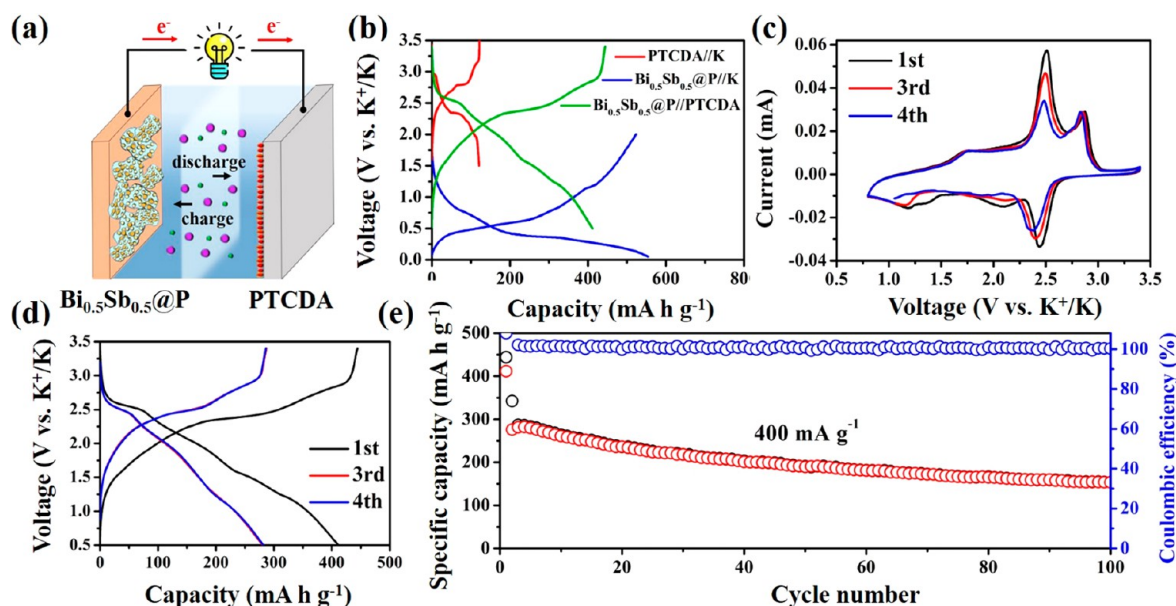


Figure 9. (a) KIB full cell using a $\text{Bi}_{0.5}\text{Sb}_{0.5}@P$ anode and a PTCDA cathode. (b) Charge/discharge curves of PTCDA, the $\text{Bi}_{0.5}\text{Sb}_{0.5}@P$ anode, and $\text{Bi}_{0.5}\text{Sb}_{0.5}@P // \text{PTCDA}$ coin full cells. (c) CV and (d) galvanostatic charge/discharge curves. (e) Electrochemical cycling performance at 400 mA g^{-1} . The specific capacity and the current density were calculated based on the mass of $\text{Bi}_{0.5}\text{Sb}_{0.5}@P$.

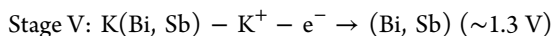
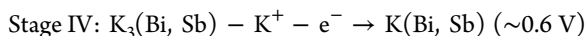
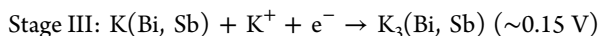
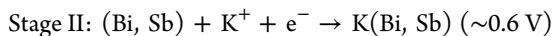
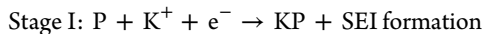
ball-milled $\text{Bi}_{0.5}\text{Sb}_{0.5}$ is more complex than that of $\text{Bi}_{0.5}\text{Sb}_{0.5}@P$. These unstable electrochemical reactions of ball-milled $\text{Bi}_{0.5}\text{Sb}_{0.5}@P$ with K^+ ions may cause structural instability and pulverization of the electrode and uncontrolled growth of the SEI layer during the charging/discharging process. This results in electrolyte consumption and increased electrode resistance. Figure S15 shows the long-term cyclability of the ball-milled $\text{Bi}_{0.5}\text{Sb}_{0.5}$ electrodes. The average Coulombic efficiency of the electrodes is 98.5% per cycle, which is lower than that (99.47% per cycle) of the $\text{Bi}_{0.5}\text{Sb}_{0.5}@P$ electrode. After 50 cycles, the average loss capacity is 1 mA h g^{-1} per cycle, far greater than the 0.12 mA h g^{-1} loss per cycle of the $\text{Bi}_{0.5}\text{Sb}_{0.5}@P$ electrode. Additionally, the cell is short-circuited after 280 cycles. Figure S16 shows an SEM image of the ball-milled $\text{Bi}_{0.5}\text{Sb}_{0.5}$ after 280 cycles. The morphology of the electrode changes significantly after cycling. The recycled $\text{Bi}_{0.5}\text{Sb}_{0.5}@P$ electrode exhibits good structural integrity (Figure 7). However, the cycled electrode material exhibits poor integrity, as evidenced by the breakage of the material into small pieces and coverage (of the material) with a thick SEI layer. These results show that the electrode stability of the ball-milled $\text{Bi}_{0.5}\text{Sb}_{0.5}$ is poor. Therefore, in terms of electrochemical stability, $\text{Bi}_{0.5}\text{Sb}_{0.5}@P$ exhibits superior structural advantage over the ball-milled $\text{Bi}_{0.5}\text{Sb}_{0.5}$ materials and excellent behavioral cycling characteristics.

To explain the potassium storage mechanism upon K^+ ion insertion and extraction, *in situ* contour mapping and XRD line plots are used to observe the structural transition and phase evolution of $\text{Bi}_{0.5}\text{Sb}_{0.5}@P$ during the first three discharge/charge processes. Figure 8a shows the *in situ* mapping XRD pattern of a live $\text{Bi}_{0.5}\text{Sb}_{0.5}@P$ half cell (left column) and the corresponding charge–discharge profile (right column). The proposed potassiation–depotassiation mechanism and the line plots of the operando XRD results obtained for the first three cycles are shown in Figures 8b and 8c–e, respectively. The experimental and calculation results of the (Bi, Sb), $\text{K}(\text{Bi, Sb})$, and $\text{K}_3(\text{Bi, Sb})$ phases are compared in Figures 8f–h. When the electrodes discharge from 2.0 V, the peak occurring at 27.7° associated with (Bi, Sb) becomes weaker than the strong

peaks corresponding to the pristine material and moves slightly toward smaller angles. This indicates that K^+ ion insertion into (Bi, Sb) crystals has started. When discharged to 0.6 V, the alloying reaction occurs. Two new peak positions at ~ 31.2 and 32.6° , which can be indexed to the (311) facet and (222) facet, respectively, of $\text{K}(\text{Bi, Sb})$, are observed. This confirms that the electrode was transformed from (Bi, Sb) to $\text{K}(\text{Bi, Sb})$ at this stage. During the discharge process, when the voltage further drops to 0.15 V, two peaks occur at 29.8 and 34.7° , corresponding to the (220) and (311) planes of $\text{K}_3(\text{Bi, Sb})$, respectively. However, the intensity of the $\text{K}(\text{Bi, Sb})$ phase decreases, thereby confirming that the alloy reaction transforming $\text{K}(\text{Bi, Sb})$ to $\text{K}_3(\text{Bi, Sb})$ occurs at this stage. The lattice parameters (*a* and *c*) calculated from XRD patterns are listed in Table S1 (Supporting Information). The potassium alloy reaction is completed through the above-mentioned processes. During the charging process, the depotassiation reaction proceeds when the voltage increases from 0.15 V. The intensity of $\text{K}_3(\text{Bi, Sb})$ decreases gradually and shifts slightly to a larger angle (than the initial angle), indicating that the K^+ ions exit the (Bi, Sb) crystal at this stage. When the voltage increases to 0.6 V, the peak corresponding to $\text{K}_3(\text{Bi, Sb})$ disappears completely, and the peak of $\text{K}(\text{Bi, Sb})$ reappears. When the voltage increases further to 1.3 V, the peak corresponding to the (012) facet of (Bi, Sb) reappears. The overall charging process and the discharging process are completely reversed. During the second and third cycles, the relationship between the changes in the peaks and the positions of the voltage is exactly the same as that of the curve obtained for the first cycle. Therefore, the potassiation–depotassiation process of the (Bi, Sb) alloys is also a reversible reaction during the second and third cycles. The weak peak appearing at an angle of 25.4° may correspond to the (112) facet of KP. The peak intensity of KP is very weak during the three cycles, indicating that this reaction is irreversible. Therefore, the results of *in situ* XRD and the elemental analysis ($\sim 9 \text{ wt } \%$ in the whole electrode) conducted via TGA and EDS indicate that phosphorus contributes an irreversible

and negligible capacity in the first discharge process. Thus, the resulting capacity obtained from the $\text{Bi}_{0.5}\text{Sb}_{0.5}@P$ electrode is mainly due to the reversible reaction of $\text{Bi}_{0.5}\text{Sb}_{0.5}$ with K^+ ions.

According to the results of the *in situ* XRD combined battery cycle in the above three cycles, the overall process of potassiation–depotassiation can be divided into five stages, as summarized below



Based on the above results, the proposed stages and corresponding capacities are summarized in Figure 8b. Irreversible reactions including the response of SEI and the response of P to KP occur in stage I, the very beginning of the discharge process from 2 V. In stage II, *i.e.*, for discharge voltages ranging from 2 to 0.6 V, K^+ ions become incorporated into the (Bi, Sb) crystal, and the initial process of alloying reaction begins. When the discharge reaches 0.6 V, (Bi, Sb) is completely transformed to $\text{K}(\text{Bi, Sb})$ with potassium ion alloying. An interval voltage range of 0.6 to 0.15 V in stage III leads to an alloying reaction, which, upon continuous K^+ ion insertion, completely transforms $\text{K}(\text{Bi, Sb})$ into $\text{K}_3(\text{Bi, Sb})$. In stage IV in the charging reaction, the voltage increased from 0.15 to 0.6 V, and the depotassiation of $\text{K}_3(\text{Bi, Sb})$ was ionized to form $\text{K}(\text{Bi, Sb})$. (Bi, Sb) crystals are reformed at ~ 1.3 V in this stage. The *in situ* XRD patterns corresponding to the first three cycles reveal that the potassiation–depotassiation reactions occurring in stages II to V are reversible reactions. Furthermore, regarding the potassiation–depotassiation process of K^+ ions reacting with $\text{Bi}_{1.11}\text{Sb}_{0.89}\text{S}_3$ nanotubes and $\text{BiSb}@C$ nanocomposites, the reported reaction pathway of K^+ ions with $\text{Bi}_{0.5}\text{Sb}_{0.5}@P$ is simpler than previously reported pathways. For example, the potassiation–depotassiation process of $\text{Bi}_{1.11}\text{Sb}_{0.89}\text{S}_3$ nanotubes involves six successive stages where involved irreversible reactions induce the decomposition of $(\text{BiSb})_2\text{S}_3$ into Bi, Sb, and K_2S_4 . This decomposition is followed by *in situ* alloying of Bi and Sb. $\text{BiSb}@C$ nanocomposites undergo seven steps of the potassiation–depotassiation process, which involve irreversible reactions of (Bi, Sb) to $\text{K}_3(\text{Bi, Sb})$ and $\text{K}(\text{Bi, Sb})$.^{32,33,36}

We paired a PTCDA cathode with a $\text{Bi}_{0.5}\text{Sb}_{0.5}@P$ anode to construct a potassium ion full cell for demonstrating the feasibility as a KIB full cell anode.^{60,61} Figure 9a shows a schematic of the full cell configuration, and Figure S18 (Supporting Information) provides a detailed analysis of PTCDA, including electrochemical evaluation of the half cell. Based on the charge/discharge curve, a PTCDA cathode provides $119.7 \text{ mA h g}^{-1}$ at 500 mA g^{-1} and working voltages ranging from 1.5 to 3.5 V. The electrolyte solution used in the full cell is 4 M KFSI in DME, and the charge/discharge voltage interval ranges from 0.5 to 3.4 V. The charging curve of the $\text{Bi}_{0.5}\text{Sb}_{0.5}@P//\text{PTCDA}$ full cell should occur in this interval, as revealed by the individual half cell charge and discharge profiles of $\text{Bi}_{0.5}\text{Sb}_{0.5}@P$ and PTCDA. Two plateaus ranging from 2.0 to 2.5 V and 2.7 to 2.9 V occur in this curve (Figure 9b), *i.e.*, the voltage curve of the $\text{Bi}_{0.5}\text{Sb}_{0.5}@P//\text{PTCDA}$ full cell corresponding to Figure 9d. The voltage curve reveals two

prominent plateaus in the charge and discharge curves. The difference between the voltage values obtained from the charging/discharging voltage profile of the full cell is ~ 2.9 V, which is similar to the difference between the voltage of the PTCDA cathode (3.5 V) and the charging voltage of $\text{Bi}_{0.5}\text{Sb}_{0.5}@P$ (0.55 V). A pair of different redox *versus* CV curves show 2.5/2.85 V in the third and fourth cycles, and the overlapping shape in the cycles indicates the good reversibility and stability of the $\text{Bi}_{0.5}\text{Sb}_{0.5}@P//\text{PTCDA}$ full cell (Figure 9c). The cell exhibits a long-term cycle life (Figure 9e), where an initial specific discharge capacity of 280 mA h g^{-1} (based on the mass of active materials) is provided. Furthermore, a reversible discharge specific capacity of 154 mA h g^{-1} after 100 cycles at 400 mA g^{-1} is maintained. The lower capacity (154 mA h g^{-1}) shows that the $\text{Bi}_{0.5}\text{Sb}_{0.5}@P$ specific capacity of the full cell is lower than that of the half cell. This results from the mismatching between the lower charging voltage in the full cell (~ 1.0 V relative to K^+/K) and the positive and negative capacities. The performance of the full cells can be further improved by optimizing the capacity balance between anode and cathode materials. The above full battery results indicate that $\text{Bi}_{0.5}\text{Sb}_{0.5}@P$ anodes are quite promising for future KIBs.

CONCLUSIONS

A solution precipitation method is used to synthesize $\text{Bi}_x\text{Sb}_{1-x}@P$ nanocomposites with the entire stoichiometry of the Bi/Sb ratio inside the P matrix. The optimally tuned Bi–Sb composition can maximize a buffering effect for large volume changes during the potassiation–depotassiation process. $\text{Bi}_{0.5}\text{Sb}_{0.5}@P$ nanocrystal electrodes exhibit 1000-cycle stability and allow ultrafast potassium ion insertion and extraction of (Bi, Sb). The potassium storage mechanism of these electrodes occurs *via* a simple, direct, and reversible reaction pathway: $(\text{Bi, Sb}) \leftrightarrow \text{K}(\text{Bi, Sb}) \leftrightarrow \text{K}_3(\text{Bi, Sb})$. The ultrasmall $\text{Bi}_{0.5}\text{Sb}_{0.5}$ nanoparticles evolved after cycling provided excellent structural advantages for outstanding electrochemical performance. The P matrix plays an important role in the excellent electrochemical performance of the $\text{Bi}_{0.5}\text{Sb}_{0.5}@P$ nanocomposites. The matrix can limit the growth of $\text{Bi}_{0.5}\text{Sb}_{0.5}$ nanocrystals to sizes of <10 nm and immobilizes nanocrystals inside the composites during cycling. Furthermore, the matrix serves both as a good electron transport medium for a very high rate capability and a good intermediate layer for uniform and thin SEI layer growth. This study shows that P is a carbon-alternative buffer material for KIB anodes accounting for a low content of the active materials and is well-mixed with additive materials for high compatibility with commercial fabrication procedures.

MATERIALS AND METHODS

Materials. Bismuth(III) chloride (BiCl_3 , 99.9%) was purchased from Alfa Aesar. Antimony(III) chloride (SbCl_3 , 99%), perylene-3,4,9,10-tetracarboxylic dianhydride (PTCDA), potassium metal (98%), 1,2-dimethoxyethane (DME, anhydrous, 99.5%), toluene (anhydrous, 99.99%), and sodium carboxymethyl cellulose (NaCMC, average $M_w \approx 700\,000$) were purchased from Sigma-Aldrich. Tris(trimethylsilyl)phosphine, min. 98% ($\text{P}(\text{SiMe}_3)_3$, 10 wt % in hexanes), was purchased from STREM. Potassium bis(fluorosulfonyl) imide (KFSI, 97%) was purchased from Chemical Block. The Celgard membrane was purchased from Advantec. Super P and the coin-type cell CR2032 were purchased from Shining Energy.

Material Synthesis. $\text{Bi}_{0.5}\text{Sb}_{0.5}@P$ nanocrystals were synthesized by colloid chemical reactions under an atmosphere of argon. First, 1.72 mmol of SbCl_3 and 1.72 mmol of BiCl_3 were dispersed in 40 mL

of toluene and stirred for 1 h. Then, 3.34 mmol of $\text{P}(\text{SiMe}_3)_3$ was added dropwise into a stirred solution at room temperature. After the solution was stirred for 3 h, the black precipitate was washed with ethanol and toluene several times and thereafter separated by centrifugation. Finally, the obtained sample was dried by rotary evaporation and subjected to a tube furnace and annealed at 200 °C for 2 h with a ramp rate of 5 °C/min under Ar flow. For comparison, the $\text{Bi}_x\text{Sb}_{1-x}\text{@P}$ samples with different Bi/Sb ratios (1:3 and 3:1) were synthesized using the same method as $\text{Bi}_{0.5}\text{Sb}_{0.5}\text{@P}$ and are denoted as $\text{Bi}_{0.25}\text{Sb}_{0.75}\text{@P}$ and $\text{Bi}_{0.75}\text{Sb}_{0.25}\text{@P}$, respectively. Bi@P and Sb@P were also synthesized using the same method and corresponding metal sources. $\text{Bi}_{0.5}\text{Sb}_{0.5}$ was prepared by a ball milling method. Bi powder (99.5%, 325 mesh, Alfa Aesar) and Sb powder (99.5%, 100 mesh, Alfa Aesar) in a mole ratio of 1:1 were mixed and sealed in a stainless steel jar with stainless steel balls inside an argon-filled glovebox. After that, the stainless steel jar was put into the Planetary Ball Mill PM 100 machine and rotated at 500 rpm for 12 h.

Material Characterizations. The morphologies and the microstructure of the prepared samples were investigated using scanning electron microscopy (HITACHI-SU8010) with energy-dispersive X-ray spectroscopy (HORIBA, EX-250) and spherical aberration corrected scanning transmission electron microscopy (JEOL, ARM200F). The structure and composition were characterized using X-ray diffraction (Bruker, D8 ADVANCE) with Cu $K\alpha$ radiation, and the valence states of the samples were identified by a high-resolution X-ray photoelectron spectrometer (ULVAC-PH, PHI QuanteraII). Thermogravimetric analysis was carried out using a thermogravimetric analyzer (TA, Q50) from 50 to 800 °C with a heating rate of 10 °C/min in N_2 . The Brunauer–Emmett–Teller surface area and pore distribution plots were measured by a Micromeritics ASAP 2060. The analysis of the XRD pattern was conducted using EVA software.

Electrochemical Measurements. $\text{Bi}_x\text{Sb}_{1-x}\text{@P}$, Bi@P , and Sb@P were mixed with Super P and carboxymethyl cellulose (CMC) binder in a weight ratio of 6:2:2 and dispersed in deionized water to prepare the slurry casting on the Cu foil for the fabrication of working electrodes. The average mass loading of active material is $\sim 0.8 \text{ mg cm}^{-2}$. To prepare a PTCDA cathode, the thermally annealed PTCDA was blended with Super P and CMC in a weight ratio of 8:1:1, which was spread on an aluminum foil. The electrochemical properties of the as-prepared electrodes were evaluated by assembling CR 2032-type coin cells in the argon-filled glovebox. For the half-cell measurement, the investigated sample was used as the working electrode, potassium metal foil was used as the counter electrode, glass fiber was used as the separator, and 4 M KFSI in DME was used as the electrolyte. The cells were cycled at 50 mA g^{-1} for a few times to obtain densely packed SEI films before the stability tests at 500 mA g^{-1} . Galvanostatic charge/discharge tests were performed in a voltage range of 0.05 to 2 V for $\text{Bi}_{0.5}\text{Sb}_{0.5}\text{@P}$ and 1.5 to 3.5 V for PTCDA at different current densities on a Maccor Series 4000 battery test system. Full cells were obtained with CR-2032-type coin cells by coupling the $\text{Bi}_{0.5}\text{Sb}_{0.5}\text{@P}$ anode, PTCDA cathode, and the electrolyte of 4 M KFSI in DME and using glass fiber as the separator. Specifically, the $\text{Bi}_{0.5}\text{Sb}_{0.5}\text{@P}$ anode was activated by charging/discharging five cycles at a current density of 50 mA g^{-1} and discharged to 0.01 V before being integrated into the full cell. Galvanostatic charge/discharge tests were carried out between 0.5 and 3.4 V. Cyclic voltammetry (CV) tests and electrochemical impedance spectroscopy (EIS) were performed on a Biologic VMP3 electrochemistry workstation.

The operando XRD patterns of $\text{Bi}_{0.5}\text{Sb}_{0.5}\text{@P}$ were collected on Bruker D8 ADVANCE diffractometer (Cu $K\alpha$) for three cycles. The investigated sample was used as the working electrode, potassium metal foil was used as the counter electrode and reference electrode, and 4 M KFSI in DME was used as the electrolyte. A current density of 50 mA g^{-1} is selected for charging and discharging processes between 0.05–2 V ($\nu\text{s K}^+/\text{K}$).

ASSOCIATED CONTENT


Supporting Information

The Supporting Information is available free of charge at <https://pubs.acs.org/doi/10.1021/acsnano.0c04203>.

Crystal structure parameters of Bi, Sb, $\text{Bi}_{0.5}\text{Sb}_{0.5}$, $\text{K}(\text{Bi,Sb})$, and $\text{K}_3(\text{Bi,Sb})$; calculated lattice parameters of $\text{Bi}_x\text{Sb}_{1-x}\text{@P}$ nanocomposites; TEM images, Raman spectra, and EDS analysis of $\text{Bi}_{0.5}\text{Sb}_{0.5}\text{@P}$ nanocomposites; TGA analysis, XPS spectrum, and BET measurement of $\text{Bi}_{0.25}\text{Sb}_{0.75}\text{@P}$ and $\text{Bi}_{0.75}\text{Sb}_{0.25}\text{@P}$ nanocomposites; the voltage profiles of the electrochemical performance of $\text{Bi}_x\text{Sb}_{1-x}\text{@P}$ nanocomposites; Nyquist plots of $\text{Bi}_{0.5}\text{Sb}_{0.5}\text{@P}$ composites; SEM images of the $\text{Bi}_{0.5}\text{Sb}_{0.5}\text{@P}$ electrode before cycling; electrochemical cycling performance of PTCDA KIB cathodes (PDF)

AUTHOR INFORMATION

Corresponding Author

Hsing-Yu Tuan – Department of Chemical Engineering,
National Tsing Hua University, Hsinchu 30013, Taiwan;
 orcid.org/0000-0003-2819-2270; Phone: (886)3-571-5131 ext: 42509; Email: hytuan@che.nthu.edu

Author

Kuan-Ting Chen – Department of Chemical Engineering,
National Tsing Hua University, Hsinchu 30013, Taiwan

Complete contact information is available at:
<https://pubs.acs.org/doi/10.1021/acsnano.0c04203>

Notes

The authors declare no competing financial interest.

ACKNOWLEDGMENTS

This work was financially supported from the Young Scholar Fellowship Program by the Ministry of Science and Technology in Taiwan, under the Grants of MOST 108-2636-E-007-013, MOST 108-2622-8-007-016, and MOST 109-2636-E-007-011. The authors also acknowledge the financial support of National Tsing Hua University through the grant of 107Q2708E1.

REFERENCES

- (1) Shannon, R. D. Revised Effective Ionic Radii and Systematic Studies of Interatomic Distances in Halides and Chalcogenides. *Acta Crystallogr., Sect. A: Cryst. Phys., Diffr., Theor. Gen. Crystallogr.* **1976**, *32*, 751–767.
- (2) Qin, M.; Ren, W.; Meng, J.; Wang, X.; Yao, X.; Ke, Y.; Li, Q.; Mai, L. Realizing Superior Prussian Blue Positive Electrode for Potassium Storage via Ultrathin Nanosheet Assembly. *ACS Sustainable Chem. Eng.* **2019**, *7*, 11564–11570.
- (3) Gao, H.; Zhou, T.; Zheng, Y.; Zhang, Q.; Liu, Y.; Chen, J.; Liu, H.; Guo, Z. CoS Quantum Dot Nanoclusters for High-Energy Potassium-Ion Batteries. *Adv. Funct. Mater.* **2017**, *27*, 1702634.
- (4) Zhang, W.; Mao, J.; Li, S.; Chen, Z.; Guo, Z. Phosphorus-Based Alloy Materials for Advanced Potassium-Ion Battery Anode. *J. Am. Chem. Soc.* **2017**, *139*, 3316–3319.
- (5) Zou, X.; Xiong, P.; Zhao, J.; Hu, J.; Liu, Z.; Xu, Y. Recent Research Progress in Non-Aqueous Potassium-Ion Batteries. *Phys. Chem. Chem. Phys.* **2017**, *19*, 26495–26506.
- (6) Suo, G.; Zhang, J.; Li, D.; Yu, Q.; Wang, W. A.; He, M.; Feng, L.; Hou, X.; Yang, Y.; Ye, X.; et al. N-Doped Carbon/Ultrathin 2D Metallic Cobalt Selenide Core/Sheath Flexible Framework Bridged by Chemical Bonds for High-Performance Potassium Storage. *Chem. Eng. J.* **2020**, *388*, 124396.

- (7) Chong, S.; Wu, Y.; Liu, C.; Chen, Y.; Guo, S.; Liu, Y.; Cao, G. Cryptomelane-Type MnO₂/Carbon Nanotube Hybrids as Bifunctional Electrode Material for High Capacity Potassium-Ion Full Batteries. *Nano Energy* **2018**, *54*, 106–115.
- (8) An, Y.; Tian, Y.; Ci, L.; Xiong, S.; Feng, J.; Qian, Y. Micron-Sized Nanoporous Antimony with Tunable Porosity for High-Performance Potassium-Ion Batteries. *ACS Nano* **2018**, *12*, 12932–12940.
- (9) Cao, L.; Zhang, B.; Xia, H.; Wang, C.; Luo, B.; Fan, X.; Zhang, J.; Ou, X. Hierarchical Chrysanthemum-Like MoS₂/Sb Heterostructure Encapsulated into N-Doped Graphene Framework for Superior Potassium-Ion Storage. *Chem. Eng. J.* **2020**, *387*, 124060.
- (10) Zhao, J.; Zou, X.; Zhu, Y.; Xu, Y.; Wang, C. Electrochemical Intercalation of Potassium into Graphite. *Adv. Funct. Mater.* **2016**, *26*, 8103–8110.
- (11) Jian, Z.; Luo, W.; Ji, X. Carbon Electrodes for K-Ion Batteries. *J. Am. Chem. Soc.* **2015**, *137*, 11566–11569.
- (12) Chang, W. C.; Wu, J. H.; Chen, K. T.; Tuan, H. Y. Red Phosphorus Potassium-Ion Battery Anodes. *Adv. Sci.* **2019**, *6*, 1801354.
- (13) Chang, W.-C.; Tseng, K.-W.; Tuan, H.-Y. Solution Synthesis of Iodine-Doped Red Phosphorus Nanoparticles for Lithium-Ion Battery Anodes. *Nano Lett.* **2017**, *17*, 1240–1247.
- (14) Chuang, C.-C.; Hsieh, Y.-Y.; Chang, W.-C.; Tuan, H.-Y. Phosphorus-Sulfur/Graphene Composites as Flexible Lithium-Sulfur Battery Cathodes with Super High Volumetric Capacity. *Chem. Eng. J.* **2020**, *387*, 123904.
- (15) Yi, Z.; Lin, N.; Zhang, W.; Wang, W.; Zhu, Y.; Qian, Y. Preparation of Sb Nanoparticles in Molten Salt and Their Potassium Storage Performance and Mechanism. *Nanoscale* **2018**, *10*, 13236–13241.
- (16) Cheng, N.; Zhao, J.; Fan, L.; Liu, Z.; Chen, S.; Ding, H.; Yu, X.; Liu, Z.; Lu, B. Sb-MOFs Derived Sb Nanoparticles@Porous Carbon for High Performance Potassium-Ion Batteries Anode. *Chem. Commun.* **2019**, *55*, 12511–12514.
- (17) Wu, Z.; Liang, G.; Pang, W. K.; Zhou, T.; Cheng, Z.; Zhang, W.; Liu, Y.; Johannessen, B.; Guo, Z. Coupling Topological Insulator SnSb₂Te₄ Nanodots with Highly Doped Graphene for High-Rate Energy Storage. *Adv. Mater.* **2020**, *32*, 1905632.
- (18) Ge, X.; Liu, S.; Qiao, M.; Du, Y.; Li, Y.; Bao, J.; Zhou, X. Enabling Superior Electrochemical Properties for Highly Efficient Potassium Storage by Impregnating Ultrafine Sb Nanocrystals within Nanochannel-Containing Carbon Nanofibers. *Angew. Chem.* **2019**, *131*, 14720–14725.
- (19) Han, Y.; Li, T.; Li, Y.; Tian, J.; Yi, Z.; Lin, N.; Qian, Y. Stabilizing Antimony Nanocrystals within Ultrathin Carbon Nanosheets for High-Performance K-Ion Storage. *Energy Storage Mater.* **2019**, *20*, 46–54.
- (20) Liu, Q.; Fan, L.; Ma, R.; Chen, S.; Yu, X.; Yang, H.; Xie, Y.; Han, X.; Lu, B. Super Long-Life Potassium-Ion Batteries Based on an Antimony@Carbon Composite Anode. *Chem. Commun.* **2018**, *54*, 11773–11776.
- (21) Bharadwaj, S.; Varma, M. C.; Singampalli, R. Antimony-Based Electrodes for Potassium Ion Batteries. *Potassium-ion Batteries: Materials and Applications* **2020**, 19–41.
- (22) Tian, Y.; An, Y.; Xiong, S.; Feng, J.; Qian, Y. A General Method for Constructing Robust, Flexible and Freestanding MXene@Metal Anodes for High-Performance Potassium-Ion Batteries. *J. Mater. Chem. A* **2019**, *7*, 9716–9725.
- (23) Luo, W.; Li, F.; Zhang, W.; Han, K.; Gaumet, J.-J.; Schaefer, H.-E.; Mai, L. Encapsulating Segment-Like Antimony Nanorod in Hollow Carbon Tube as Long-Lifespan, High-Rate Anodes for Rechargeable K-Ion Batteries. *Nano Res.* **2019**, *12*, 1025–1031.
- (24) Huang, Z.; Chen, Z.; Ding, S.; Chen, C.; Zhang, M. Multi-Protection from Nanochannels and Graphene of SnSb-Graphene-Carbon Composites Ensuring High Properties for Potassium-Ion Batteries. *Solid State Ionics* **2018**, *324*, 267–275.
- (25) Liu, Z.; Song, T.; Paik, U. Sb-Based Electrode Materials for Rechargeable Batteries. *J. Mater. Chem. A* **2018**, *6*, 8159–8193.
- (26) Ding, H.; Wang, J.; Fan, L.; Liu, Z.; Jia, X.; Yu, X.; Lu, B. Sn-Sb Compounds with Novel Structure for Stable Potassium Storage. *Chem. Eng. J.* **2020**, *395*, 125147.
- (27) Zhang, Y.; Li, M.; Huang, F.; Li, Y.; Xu, Y.; Wang, F.; Yao, Q.; Zhou, H.; Deng, J. 3D Porous Sb-Co Nanocomposites as Advanced Anodes for Sodium-Ion Batteries and Potassium-Ion Batteries. *Appl. Surf. Sci.* **2020**, *499*, 143907.
- (28) Wang, Z.; Dong, K.; Wang, D.; Luo, S.; Liu, Y.; Wang, Q.; Zhang, Y.; Hao, A.; Shi, C.; Zhao, N. A Nanosized SnSb Alloy Confined in N-Doped 3D Porous Carbon Coupled with Ether-Based Electrolytes toward High-Performance Potassium-Ion Batteries. *J. Mater. Chem. A* **2019**, *7*, 14309–14318.
- (29) Zhao, Y.; Manthiram, A. High-Capacity, High-Rate Bi–Sb Alloy Anodes for Lithium-Ion and Sodium-Ion Batteries. *Chem. Mater.* **2015**, *27*, 3096–3101.
- (30) Gao, H.; Niu, J.; Zhang, C.; Peng, Z.; Zhang, Z. A Dealloying Synthetic Strategy for Nanoporous Bismuth–Antimony Anodes for Sodium Ion Batteries. *ACS Nano* **2018**, *12*, 3568–3577.
- (31) He, X.-D.; Liao, J.-Y.; Wang, S.; Wang, J.-R.; Liu, Z.-H.; Ding, X.; Hu, Q.; Wen, Z.-Y.; Chen, C.-H. From Nanomelting to Nanobeads: Nanostructured Sb_xBi_{1-x} Alloys Anchored in Three-Dimensional Carbon Frameworks as a High-Performance Anode for Potassium-Ion Batteries. *J. Mater. Chem. A* **2019**, *7*, 27041–27047.
- (32) Wang, J.; Wang, B.; Lu, B. Nature of Novel 2D van der Waals Heterostructures for Superior Potassium Ion Batteries. *Adv. Energy Mater.* **2020**, *10*, 2000884.
- (33) Xiong, P.; Wu, J.; Zhou, M.; Xu, Y. Bismuth-Antimony Alloy Nanoparticle@Porous Carbon Nanosheet Composite Anode for High Performance Potassium-Ion Batteries. *ACS Nano* **2020**, *14*, 1018–1026.
- (34) Guo, S.; Li, H.; Lu, Y.; Liu, Z.; Hu, X. Lattice Softening Enables Highly Reversible Sodium Storage in Anti-Pulverization Bi–Sb Alloy/Carbon Nanofibers. *Energy Storage Mater.* **2020**, *27*, 270–278.
- (35) Chu, J.; Wang, W. A.; Yu, Q.; Lao, C.-Y.; Zhang, L.; Xi, K.; Han, K.; Xing, L.; Song, L.; Wang, M.; et al. Open ZnSe/C Nanocages: Multi-Hierarchy Stress-Buffer for Boosting Cycling Stability in Potassium-Ion Batteries. *J. Mater. Chem. A* **2020**, *8*, 779–788.
- (36) Wang, J.; Fan, L.; Liu, Z.; Chen, S.; Zhang, Q.; Wang, L.; Yang, H.; Yu, X.; Lu, B. *In Situ* Alloying Strategy for Exceptional Potassium Ion Batteries. *ACS Nano* **2019**, *13*, 3703–3713.
- (37) Liu, D.; Yang, L.; Chen, Z.; Zou, G.; Hou, H.; Hu, J.; Ji, X. Ultra-Stable Sb Confined into N-Doped Carbon Fibers Anodes for High-Performance Potassium-Ion Batteries. *Sci. Bull.* **2020**, *65*, 1003–1012.
- (38) Zhang, W.; Miao, W.; Liu, X.; Li, L.; Yu, Z.; Zhang, Q. High-Rate and Ultralong-Stable Potassium-Ion Batteries Based on Antimony-Nanoparticles Encapsulated in Nitrogen and Phosphorus Co-Doped Mesoporous Carbon Nanofibers as an Anode Material. *J. Alloys Compd.* **2018**, *769*, 141–148.
- (39) Wang, Z.; Dong, K.; Wang, D.; Luo, S.; Liu, X.; Liu, Y.; Wang, Q.; Zhang, Y.; Hao, A.; He, C.; et al. Constructing N-Doped Porous Carbon Confined FeSb Alloy Nanocomposite with Fe-NC Coordination as a Universal Anode for Advanced Na/K-Ion Batteries. *Chem. Eng. J.* **2020**, *384*, 123327.
- (40) Choi, I. Y.; Jo, C.; Lim, W.-G.; Han, J.-C.; Chae, B.-G.; Park, C. G.; Lee, J.; Kim, J. K. Amorphous Tin Oxide Nanohelix Structure Based Electrode for Highly Reversible Na-Ion Batteries. *ACS Nano* **2019**, *13*, 6513–6521.
- (41) Zhang, Z.; Wang, Z. L.; Lu, X. Multishelled Si@Cu Microparticles Supported on 3D Cu Current Collectors for Stable and Binder-Free Anodes of Lithium-Ion Batteries. *ACS Nano* **2018**, *12*, 3587–3599.
- (42) Yang, J.; Ju, Z.; Jiang, Y.; Xing, Z.; Xi, B.; Feng, J.; Xiong, S. Enhanced Capacity and Rate Capability of Nitrogen/Oxygen Dual-Doped Hard Carbon in Capacitive Potassium-Ion Storage. *Adv. Mater.* **2018**, *30*, 1700104.
- (43) An, Y.; Tian, Y.; Wei, H.; Xi, B.; Xiong, S.; Feng, J.; Qian, Y. Porosity-and Graphitization-Controlled Fabrication of Nanoporous

Silicon@Carbon for Lithium Storage and Its Conjugation with MXene for Lithium-Metal Anode. *Adv. Funct. Mater.* **2020**, *30*, 1908721.

(44) Stokes, K.; Geaney, H.; Sheehan, M.; Borsa, D.; Ryan, K. M. Copper Silicide Nanowires as Hosts for Amorphous Si Deposition as a Route to Produce High Capacity Lithium-Ion Battery Anodes. *Nano Lett.* **2019**, *19*, 8829–8835.

(45) Stokes, K.; Boonen, W.; Geaney, H.; Kennedy, T.; Borsa, D.; Ryan, K. M. Tunable Core–Shell Nanowire Active Material for High Capacity Li-Ion Battery Anodes Comprised of PECVD Deposited aSi on Directly Grown Ge Nanowires. *ACS Appl. Mater. Interfaces* **2019**, *11*, 19372–19380.

(46) Allen, G. C.; Carmalt, C. J.; Cowley, A. H.; Hector, A. L.; Kamepalli, S.; Lawson, Y. G.; Norman, N. C.; Parkin, I. P.; Pickard, L. K. Preparation and Characterization of a Material of Composition BiP (Bismuth Phosphide) and Other Intergroup 15 Element Phases. *Chem. Mater.* **1997**, *9*, 1385–1392.

(47) Davidson, F. M.; Wiacek, R.; Korgel, B. A. Supercritical Fluid-Liquid- Solid Synthesis of Gallium Phosphide Nanowires. *Chem. Mater.* **2005**, *17*, 230–233.

(48) Holzwarth, U.; Gibson, N. The Scherrer Equation Versus The Debye-Scherrer Equation. *Nat. Nanotechnol.* **2011**, *6*, 534–534.

(49) Vegard, L. Die Konstitution Der Mischkristalle Und Die Raumbüllung Der Atome. *Eur. Phys. J. A* **1921**, *5*, 17–26.

(50) Loor, M.; Bendt, G.; Hagemann, U.; Wölper, C.; Assenmacher, W.; Schulz, S. Synthesis of Bi₂Te₃ and (Bi_xSb_{1-x})₂Te₃ Nanoparticles Using The Novel IL [C₄ mim]₃[Bi₃I₁₂]. *Dalton Trans.* **2016**, *45*, 15326–15335.

(51) Su, S.; Liu, Q.; Wang, J.; Fan, L.; Ma, R.; Chen, S.; Han, X.; Lu, B. Control of SEI Formation for Stable Potassium-Ion Battery Anodes by Bi-MOF-Derived Nanocomposites. *ACS Appl. Mater. Interfaces* **2019**, *11*, 22474–22480.

(52) Liu, H.; Wang, Z.; Wu, Z.; Zhang, S.; Ge, S.; Guo, P.; Hua, M.; Lu, X.; Wang, S.; Zhang, J. Direct Tuning of Meso-/Micro-Porous Structure of Carbon Nanofibers Confining Sb Nanocrystals for Advanced Sodium and Potassium Storage. *J. Alloys Compd.* **2020**, *833*, 155127.

(53) Kim, S. S.; Britcher, L.; Kumar, S.; Griesser, H. J. XPS Study of Sulfur and Phosphorus Compounds with Different Oxidation States. *Sains Malays.* **2018**, *47*, 1913–1922.

(54) Huang, H.; Xiao, Q.; Wang, J.; Yu, X.-F.; Wang, H.; Zhang, H.; Chu, P. K. Black Phosphorus: a Two-Dimensional Reductant for *In Situ* Nanofabrication. *NPJ. 2D Mater. Appl.* **2017**, *1*, 20.

(55) Cao, K.; Liu, H.; Jia, Y.; Zhang, Z.; Jiang, Y.; Liu, X.; Huang, K. J.; Jiao, L. Flexible Antimony@ Carbon Integrated Anode for High-Performance Potassium-Ion Battery. *Adv. Mater. Technol.* **2020**, *5*, 2000199.

(56) Lindström, H.; Södergren, S.; Solbrand, A.; Rensmo, H.; Hjelm, J.; Hagfeldt, A.; Lindquist, S.-E. Li⁺ Ion Insertion in TiO₂ (Anatase). 2. Voltammetry on Nanoporous Films. *J. Phys. Chem. B* **1997**, *101*, 7717–7722.

(57) Xia, X.; Chao, D.; Zhang, Y.; Zhan, J.; Zhong, Y.; Wang, X.; Wang, Y.; Shen, Z. X.; Tu, J.; Fan, H. J. Generic Synthesis of Carbon Nanotube Branches on Metal Oxide Arrays Exhibiting Stable High-Rate and Long-Cycle Sodium-Ion Storage. *Small* **2016**, *12*, 3048–3058.

(58) Kim, H.-S.; Cook, J. B.; Lin, H.; Ko, J. S.; Tolbert, S. H.; Ozolins, V.; Dunn, B. Oxygen Vacancies Enhance Pseudocapacitive Charge Storage Properties of MoO_{3-x}. *Nat. Mater.* **2017**, *16*, 454–460.

(59) Liu, L.; An, M.; Yang, P.; Zhang, J. Superior Cycle Performance and High Reversible Capacity of SnO₂/Graphene Composite as an Anode Material for Lithium-Ion Batteries. *Sci. Rep.* **2015**, *5*, 9055.

(60) Chen, Y.; Luo, W.; Carter, M.; Zhou, L.; Dai, J.; Fu, K.; Lacey, S.; Li, T.; Wan, J.; Han, X.; et al. Organic Electrode for Non-Aqueous Potassium-Ion Batteries. *Nano Energy* **2015**, *18*, 205–211.

(61) Fan, L.; Ma, R.; Wang, J.; Yang, H.; Lu, B. An Ultrafast and Highly Stable Potassium–Organic Battery. *Adv. Mater.* **2018**, *30*, 1805486.